

Report Documentation Page			Form Approved OMB No. 0704-0188		
Public reporting burden for the collection of information is estimated to average 1 hour per response, including the time for reviewing instructions, searching existing data sources, gathering and maintaining the data needed, and completing and reviewing the collection of information. Send comments regarding this burden estimate or any other aspect of this collection of information, including suggestions for reducing this burden, to Washington Headquarters Services, Directorate for Information Operations and Reports, 1215 Jefferson Davis Highway, Suite 1204, Arlington VA 22202-4302. Respondents should be aware that notwithstanding any other provision of law, no person shall be subject to a penalty for failing to comply with a collection of information if it does not display a currently valid OMB control number.					
1. REPORT DATE 01 JUN 2012	2. REPORT TYPE		3. DATES COVERED 00-00-2012 to 00-00-2012		
4. TITLE AND SUBTITLE Linking Dynamics Of The Near-surface Flow To Deeper Boundary Layer Forcing In The Nocturnal Boundary Layer			5a. CONTRACT NUMBER		
			5b. GRANT NUMBER		
			5c. PROGRAM ELEMENT NUMBER		
6. AUTHOR(S)			5d. PROJECT NUMBER		
			5e. TASK NUMBER		
			5f. WORK UNIT NUMBER		
7. PERFORMING ORGANIZATION NAME(S) AND ADDRESS(ES) Oregon State University,Corvallis,OR,97331			8. PERFORMING ORGANIZATION REPORT NUMBER		
9. SPONSORING/MONITORING AGENCY NAME(S) AND ADDRESS(ES)			10. SPONSOR/MONITOR'S ACRONYM(S)		
			11. SPONSOR/MONITOR'S REPORT NUMBER(S)		
12. DISTRIBUTION/AVAILABILITY STATEMENT Approved for public release; distribution unlimited					
13. SUPPLEMENTARY NOTES					
14. ABSTRACT					
15. SUBJECT TERMS					
16. SECURITY CLASSIFICATION OF:			17. LIMITATION OF ABSTRACT Same as Report (SAR)	18. NUMBER OF PAGES 87	19a. NAME OF RESPONSIBLE PERSON
a. REPORT unclassified	b. ABSTRACT unclassified	c. THIS PAGE unclassified			

AN ABSTRACT OF THE THESIS OF

Alexander R. Smoot for the degree of Master of Science in Atmospheric Science
presented on June 1st, 2012.

Title: Linking dynamics of the near-surface flow to deeper boundary layer forcing
in the nocturnal boundary layer

Abstract approved: _____

Christoph K. Thomas

Weak-wind flow in the nocturnal boundary is one of the most poorly understood problems in the field of meteorology. The understanding of weak-wind flows is essential for the improvement of regulatory dispersion models which are currently rendered invalid under weak-wind conditions and stable stratification. Recently there have been increased efforts directed towards improving the understanding nocturnal boundary layer dynamics. The results of these studies have shown that nocturnal boundary layer flows are often dominated by intermittent turbulence and motions occurring on horizontal scales ranging from hundreds of meters to several kilometers and on time scales of 1 minute to 1 hour. We refer to these scales as sub-meso. This connection has led to the hypothesis that intermittent turbulence generation may be the result of sub-meso motions that are subject to external forcing originating in the deeper boundary layer. However, these processes have proven difficult to measure as traditional sensor networks have failed to provide the vertical and horizontal coverage necessary to observe the driving forces on these scales. This study sought to close this knowledge gap using SOund Detection And Ranging (SODAR). SODAR is a ground based acoustic remote sensing technology that is capable of measuring wind and turbulence at multiple heights in the boundary layer. Data were collected with a pair of SODAR systems with sequentially increasing separation distance at the Oregon

State University Botany and Plant Pathology lab during the summer of 2010. The data have indicated that motion occurring on time scales of 2 minutes to 32 minutes are isolated to the lowest 50 meters of the nocturnal boundary layer. Surface-layer measurements were collected using a pair of sonic anemometers placed at heights of 1.5 and 7 meters above ground level. Comparisons of surface-layer measurements and deeper boundary layer measurements have shown that when the surface layer stratification is stable, processes within the surface layer are not likely to be influenced by external forcing from aloft. In contrast external forcing from the deeper boundary layer may still have an influence on weak, nocturnal surface flows when the surface layer is weakly stratified as is shown for the case of low-level jets.

©Copyright by Alexander R. Smoot

June 1st, 2012

All Rights Reserved

Linking dynamics of the near-surface flow to deeper boundary layer forcing in the
nocturnal boundary layer

by

Alexander R. Smoot

A THESIS

submitted to

Oregon State University

in partial fulfillment of
the requirements for the
degree of

Master of Science

Presented June 1st, 2012
Commencement June 2013

Master of Science thesis of Alexander R. Smoot presented on June 1st, 2012

APPROVED:

Major Professor, representing Atmospheric Science

Dean of the College of Earth, Ocean, and Atmospheric Sciences

Dean of the Graduate School

I understand that my thesis will become part of the permanent collection of Oregon State University libraries. My signature below authorizes release of my thesis to any reader upon request.

Alexander R. Smoot, Author

ACKNOWLEDGEMENTS

Academic

I am indebted to my advisor Dr. Christoph K. Thomas, his tireless attention to detail and strong work ethic provided the example I needed to accomplish the task of completing my thesis research. I also owe my degree to Dr. Eric Skyllingstad, Dr. Simon de Szoeke, and Dr. David McIntyre for serving on my committee. Finally, I am indebted to our sponsors, the National Science Foundation, and the U.S. Army Research Office.

Personal

I wish to thank members of the biomicrometeorology group for helping with field work, writing, and data analysis. Special thanks also goes to the CEOAS staff for their help throughout the degree process. Last but certainly not least, I cannot fully express my gratitude for the support my parents have given me as well as the rest of my friends and family, thank you all.

TABLE OF CONTENTS

	<u>Page</u>
1. INTRODUCTION	1
2. THEORETICAL BACKGROUND	4
2.1. Turbulent Mixing.....	4
2.1.1 Measurement of Turbulent Structures and Taylor’s Hypothesis...	4
2.2. The Atmospheric Boundary Layer	5
2.2.1 Dynamics of the stable boundary layer	7
3. MATERIALS AND METHODS	9
3.1. SODAR.....	9
3.1.1 Physical Principle.....	9
3.1.2 Data Processing and Conversion	14
3.1.3 Limitations to the SODAR technique.....	16
3.2. DONUTSS-2010 Field Experiment.....	19
3.2.1 Site Layout	19
3.2.2 SODAR Setup and User Settings.....	21
3.2.3 Checking for fixed echoes	22
3.3. Data Quality Control.....	23
3.3.1 Selecting SODAR averaging method.....	23
3.3.2 Selecting SODAR sounding frequency	26
3.3.3 Azimuth Corrections	26
4. DATA ANALYSIS TECHNIQUES	28
4.1. Multi-Resolution Decomposition.....	28
4.1.1 MRD Averaging Scheme	29
4.1.2 Modifications	30
4.1.3 Implementation	30
4.2. Post MRD filtering.....	32
4.3. Bulk Statistics.....	32

TABLE OF CONTENTS (Continued)

	<u>Page</u>
5. RESULTS & DISCUSSION	35
5.1. Near surface flow characterization	35
5.1.1 Definition of flow regimes	35
5.1.2 Mean profiles for flow regimes	36
5.1.3 Observation of directional variability as a function of upper level wind shear	38
5.2. Bulk statistics	40
5.2.1 Vertical Correlations Between Gates	41
5.2.2 Between-Station Correlations	42
5.3. Horizontal Space-Time Analysis	47
5.4. Case studies	48
5.4.1 Case #1: High variability	49
5.4.2 Case #2: Low level jet	55
6. CONCLUSIONS	61
APPENDICES	67
A APPENDIX A SODAR Spectral Analysis	68
B APPENDIX B SODAR Error Codes	72

LIST OF FIGURES

<u>Figure</u>	<u>Page</u>
2.1 Taylor's Hypothesis.....	5
2.2 Boundary layer diagram	6
2.3 Space time regime diagram	8
3.1 Phased array	13
3.2 Averaging methods	14
3.3 Classical and molecular attenuation.....	17
3.4 Site configuration.....	20
3.5 Fixed echo	23
3.6 Data quality.....	24
3.7 Averaging technique comparison	25
4.1 MRD.....	31
4.2 Cases with height	33
5.1 $\Delta\theta$ between sonics vs. V_{7m}	36
5.2 Wind speed filtering results	38
5.3 Mean profiles	39
5.4 Mid level directional variability vs upper shear	40
5.5 Mid level directional variability vs upper shear 2	41
5.6 Low level directional variability vs upper shear	42
5.7 Vertical correlation	43
5.8 Vertical space-time analysis.....	44
5.9 Station correlation with height: weak winds.....	45
5.10 Station correlation with height: strong winds	46
5.11 Horizontal correlation between stations	48

LIST OF FIGURES (Continued)

<u>Figure</u>	<u>Page</u>
5.12 08/26 - 08/27 wind profile	49
5.13 Case #1 Event I.....	50
5.14 Case #1 Event II.....	52
5.15 Case #1 Event III.....	53
5.16 Case #1 Event IV	54
5.17 10/02 - 10/03 wind profile	55
5.18 Case #2 Event I.....	56
5.19 Case #2 Event II.....	57
5.20 Case #2 Event III.....	58
5.21 Case #2 net radiation	59
5.22 Case #2 Event IV	60

LIST OF TABLES

<u>Table</u>	<u>Page</u>
3.1 Site details	20
3.2 Azimuth corrections	27
4.1 Sample MRD averaging.....	30
5.1 Critical wind filtering.....	37
0.1 Error Codes	73

LINKING DYNAMICS OF THE NEAR-SURFACE FLOW TO DEEPER BOUNDARY LAYER FORCING IN THE NOCTURNAL BOUNDARY LAYER

1. INTRODUCTION

The overarching goal of this research is to improve our understanding of near-surface, weak-wind processes and their driving forces over short vegetation and mildly heterogeneous terrain. It has been shown that in many parts of the world weak-wind conditions are prevalent for a significant percentage of time (Anfossi et al., 2005). Despite the prevalence of weak-wind conditions, the processes that occur under them are some of the most poorly understood processes in boundary layer meteorology (see Sun et al., 2004 and references therein). This knowledge gap presents considerable problems when addressing the issue of constituent and momentum transport.

Whether investigating the transport of radioactive material from a nuclear plant, the spread of contaminants from an industrial smokestack, or seed dispersal from local flora it is necessary to have an understanding of turbulent transport. This statement is true because turbulent transport dominates the dispersion and diffusion of atmospheric constituents released within the atmospheric Surface Layer (SL). Regulatory dispersion models are known to become unreliable as the average wind speed near the surface approaches zero (Anfossi et al., 2005, Lines et al., 1997). The dysfunction of the dispersion models under weak winds stems from the lack of understanding of two things:

- The generation of turbulence under weak-wind conditions which leads to vertical diffusion.

- The behavior of sub-meso scale motions which dominate the horizontal dispersion of atmospheric constituents under weak winds.

Under weak wind conditions, turbulence has been shown to disobey Taylor’s hypothesis and other similarity theories (Mahrt et al., 2009). The behavior of turbulence is intermittent under these conditions and its generation can be ambiguous. It is thought that this intermittency is due to sub-meso scale motions. In the absence of significant mean winds, the effects of sub-meso scale motion become more significant. Processes on this scale include wave-like phenomena, meandering (Anfossi et al., 2005), sudden shifts in wind direction (Mahrt, 2008b), and other complex processes existing on horizontal scales greater than turbulence but lesser than meso-gamma. Sub-meso motions were examined stochastically by Mahrt (2007, 2008b) and Mahrt et al. (2009) but with little success at characterizing sub meso motions and their non stationary effects on turbulence.

The reason that Mahrt et al. (2009) and the others have failed to characterize sub-meso motions has been the insufficient spatial coverage of traditional near-surface atmospheric sensor networks. Standard tower-mounted instruments are spatially limited due to the height of the tower. The invalidity of Taylor’s hypothesis under weak wind conditions imposes limitations as horizontal scales cannot be inferred from Eulerian time series’.

The objectives of this work are:

1. Collecting a data set consisting of wind speed data from a wide horizontal and vertical range will be obtained. This will be accomplished using ground based acoustic remote sensing (SODAR) technology which can be used to sense winds in the lower boundary layer with sufficiently high temporal resolution (see Chapter 4.).
2. Data will be decomposed into multiple time scales in order to investigate the temporal scales of near surface processes as well as forcing from aloft. This will be accomplished using a wavelet-based analyses tool called Multi-Resolution Decompo-

sition (MRD) developed by Howell and Mahrt (1997). This process is discussed in detail in Chapter 4.

3. Using correlation analyses of the decomposed data, this research will attempt to characterize the spatial and temporal scales of sub-meso scale motions under weak-wind conditions within the stable boundary layer.
4. Through observation of near surface variability, this research will investigate the connection between weak-wind surface flows and external forcing originating in the deeper boundary layer.

2. THEORETICAL BACKGROUND

2.1. Turbulent Mixing

Turbulent mixing is among the most complex areas of study within the field of meteorology. The source of the complexity lies with the blending of micro-scale molecular diffusion and larger scale (though still small) fluid dynamics. On a large scale, turbulence gains energy from mean flow dynamics, i.e., differences in the speed and direction of neighboring air parcels, and buoyancy effects. At the smallest scale, turbulent energy is dissipated based on the molecular viscosity of the air (Arya, 2001). Qualitatively, turbulence is referred to in terms of eddies, which are essentially 3-D vortices of air (not a 2 dimensional vortex but an overturning, ellipsoidal parcel of air). Turbulent eddies exist on numerous scales simultaneously. The concept of cascading turbulence, introduced by Lewis Richardson in 1922, suggests that the largest scale eddies gain energy from the mean flow while simultaneously feeding smaller eddies contained within them. These smaller eddies then feed even smaller eddies and the pattern continues down to the scale of molecular viscosity.

2.1.1 Measurement of Turbulent Structures and Taylor's Hypothesis

The measurement of turbulent eddies in the atmosphere has proven a challenge to scientists throughout the 20th century. This is due to the inability to directly observe the spatial structure of turbulent eddies. Standard methods of recording turbulence data are only able to capture data on the temporal scale, not the spatial scale. In an effort to resolve this issue, Taylor (1938) proposed a hypothesis which is commonly accepted today. Taylor's hypothesis dictates that when advective wind speeds are greater than local turbulent speeds, the spatial scale and the temporal scale of turbulent eddies are related by the mean wind speed. This concept assumes that turbulence is "frozen" meaning that

the shape of a turbulent eddy being measured does not change as it passes through the location of measurement (illustrated in Figure 2.1). Taylor's hypothesis has proven to

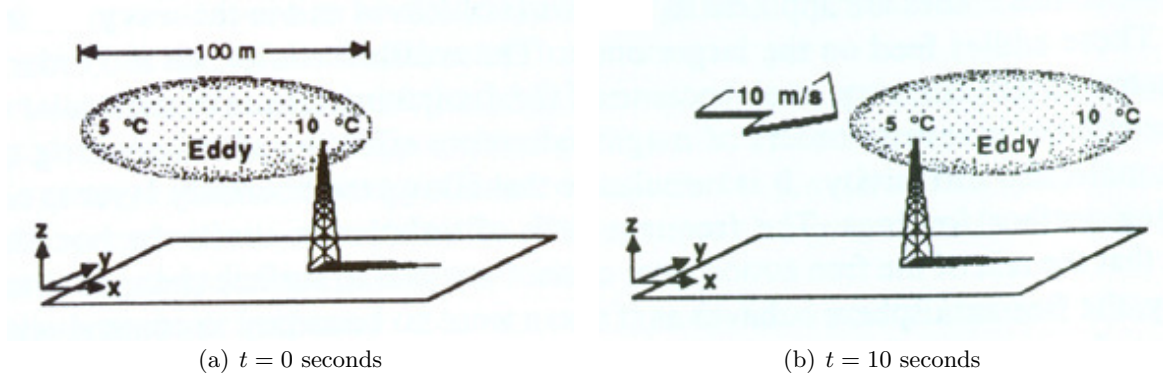


FIGURE 2.1: 2.1(a) An eddy 100 meters in diameter with a 5°C temperature difference across it. 2.1(b) The same eddy is carried by the mean wind speed to it's new position 10 seconds later. Image taken from Stull (1988).

have two major limitations. First, the presence of sufficiently large turbulent intensities, common under unstable and convective conditions, can result in the apparent effect of increasing velocity perturbations above the mean wind speed. Secondly, the presence of strong vertical shearing can result in large eddies being carried at different mean wind speeds than smaller eddies due to the wind gradient across the large eddies (Arya, 2001).

2.2. The Atmospheric Boundary Layer

The Atmospheric Boundary Layer (ABL) is defined as the layer of the atmosphere in which wind dynamics are influenced by the surface. On a clear day, the surface of the Earth is heated by the sun resulting in an unstably stratified ABL (i.e the potential temperature decreases with height). Unstable stratification causes convection due to positive buoyancy which in turn results in increased turbulence intensity throughout the ABL. The daytime ABL is often referred to as the Convective Boundary Layer (CBL) for this reason. The lowest portion of the CBL, the SL, represents the portion of the atmosphere in which the

effects of the Earth's rotation become insignificant and horizontal transport is dominated by pressure gradients and gravity effects. Above the SL is the mixed layer which is often under near neutral stratification and represents the bulk of the CBL. Finally the CBL is topped by an inversion layer which separates the turbulent ABL from the more orderly free troposphere above.

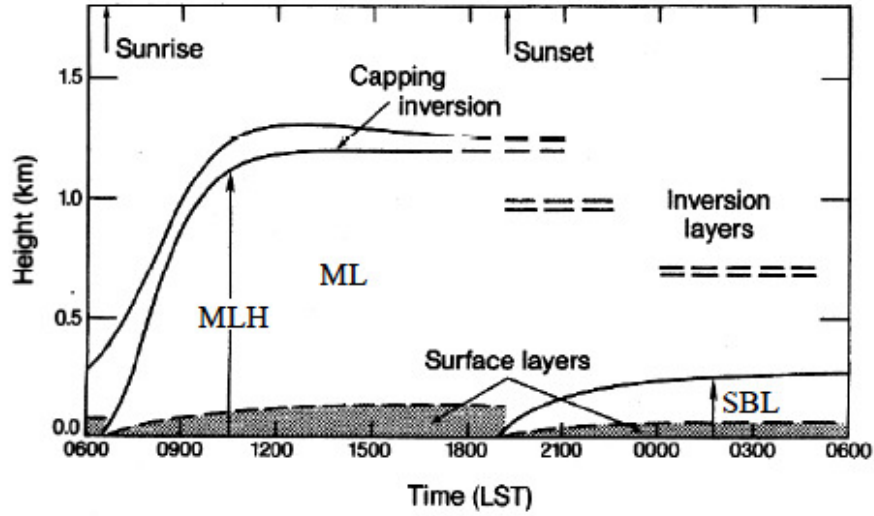


FIGURE 2.2: Image of the development of the convective and stable boundary layers over the course of a day due to the diurnal change in radiative heating. (taken from Kaimal and Finnigan (1994), modified)

Figure 2.2 illustrates the evolution from unstable CBL to a nocturnal Stable Boundary Layer (SBL) in the absence of significant synoptic scale forcing. As the day transitions into night, the surface is no longer heated by the sun causing the surface to transition from a heat source to a heat sink. Just before sunset an inversion layer begins to form at the surface due to a divergence in sensible heat flux. This inversion layer steadily deepens just after sunset and the capping inversion layer appears to sink resulting in a shrunk mixed layer. The remaining mixed layer acts as a cap for the SBL. The SBL persists through the night until sunrise when surface heating resumes and a new unstable layer begins to form at the surface, gradually returning to a CBL.

2.2.1 Dynamics of the stable boundary layer

Because the SBL is stably stratified, buoyancy effects within this layer are suppressed. This results in vanishing convective turbulence. Thus any turbulence occurring within the SBL is generated through mechanical shearing. The reduction in vertical motion caused by stable stratification results in a decrease in the momentum flux within the SBL. Weakened momentum flux, in turn, causes a significant increase in mechanical shearing as the vertical transport of kinetic energy is reduced. In time the mechanical shearing between two layers of different density can result in dynamic instability causing wave-like behavior to induce turbulence between layers. The reduction of vertical momentum flux also results in generally weaker wind speeds in the SBL as compared to the CBL. Without significant momentum flux it is common for the wind direction to be subject to sudden shifts of above 90° , a phenomenon referred to as meandering (Mahrt, 2008a,b).

The SBL generally has reduced wind speeds except in the special case of the low-level jet (LLJ), a phenomenon that is the result of large-scale flow patterns (discussed in more detail in Chapter 5 and Stull, 1988). In the absence of strong large-scale forcing, the prevalence of weak, sporadic flow patterns is increased. These flows occur on a scale that is larger than that of turbulence but smaller than 2 km, the minimum scale of meso-gamma motions. In order to avoid conflicts with the traditional use of the term *meso* we refer to these smaller scale motions as *sub-meso* (Mahrt and Mills, 2009). Figure 2.3 shows a diagram of the various nocturnal flow regimes in space and time.

In addition to weakened momentum flux in the SBL, the vertical transport of constituents is also weakened and intermittent, usually being the result of turbulence generated by shearing on sub-meso time scales. Conversely, horizontal transport in the nocturnal ABL can be quite strong (Mahrt and Mills, 2009).

Despite recent efforts to measure the extent of sub-meso scale dispersion (Mahrt, 2007, 2008b, Mahrt et al., 2009), information is still lacking in part due to insufficient

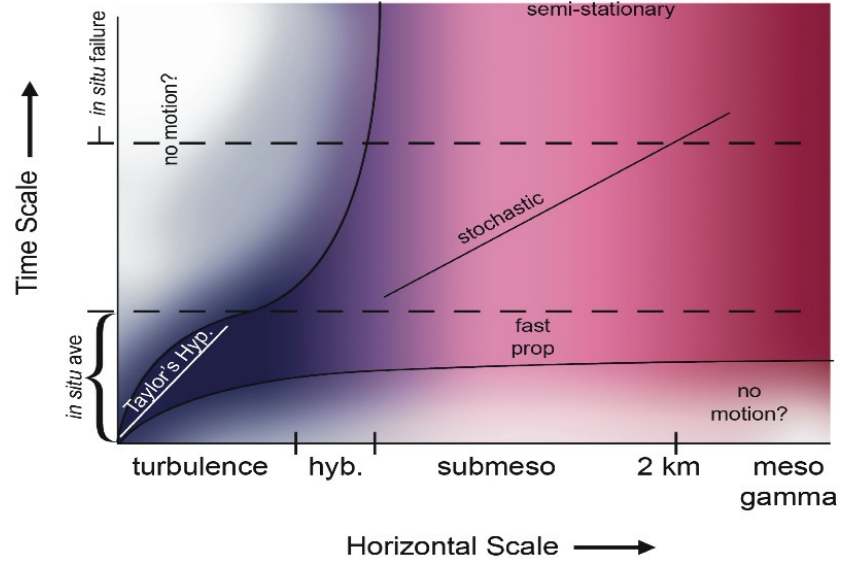


FIGURE 2.3: Diagrams of the various regimes in the space time domain. (Mahrt, 2010)

spatial coverage of sensor networks. In addition, Taylor's hypothesis cannot be used to model sub-meso motions because the evolving time scale of the individual structures is often much shorter than the advective time scale (Thomas, 2011).

3. MATERIALS AND METHODS

3.1. SODAR

The primary observational tool used to collect data for this research was a Sound Detection And Ranging (SODAR) system. A device based on the same physical principle originally documented by John Tyndall (Tyndall, 1874), who discovered the effect of sound scattering by turbulence. The principle was expanded upon by a number of scientists during the 20th century (see Blokhintzev, 1946, Kraichnan, 1953) resulting in the development of the theory of sound wave scattering. The first SODAR system was experimented with in 1964 (see Kallistratova, 1997 and references therein). Since then, SODAR technology has become a tool commonly used to study the lower ABL flow (see Argentini et al., 2012, Coulter and Kallistratova, 2004, Meyer, 2005 and references therein).

3.1.1 Physical Principle

The principle of turbulent acoustic scattering

A SODAR operates by emitting a sound pulse then measuring the properties of the backscattered sound. In order for the pulse to scatter, there needs to be a scattering medium. This is provided by small-scale density inhomogeneities found throughout the ABL. The speed of sound c in dry air can be represented using the Laplace formula and the Ideal Gas Law:

$$c = \left(\frac{\gamma RT}{\mu} \right)^{1/2} \quad (3.1)$$

When an inhomogeneity is encountered by a sound wave, some of the energy is scattered. In the real atmosphere, there is always some water vapor content which affects the atomic mass (μ) and the heat capacity ratio (γ). Hence, scattering intensity is affected by changes in air density due to advection by the mean wind, convection, turbulence generation

through shear layers, and changes in water vapor concentration (e.g. clouds). These inhomogeneities are, essentially, turbulent eddies.

The Bragg condition states the dependence of scattering intensity on sound wavelength λ and size of temperature inhomogeneities (eddies) l_t . The intensity is represented as the Bragg angle Θ_B which is equal to half of the scattering angle. The relationship between Bragg angle, turbulent eddy size, and sound wavelength is shown below (Kallistratova, 1997):

$$l_t = \frac{\lambda}{2\sin\Theta_B} \quad (3.2)$$

In the case of ideal scattering, in which the Bragg angle equals 90° , the relationship reduces to:

$$l_t = \frac{\lambda}{2} \quad (3.3)$$

Thus, maximum scattering efficiency is achieved when the size of turbulent eddies is half the wavelength of the sound pulse emitted by the SODAR. The specific equation used to predict the power of reflected sound P_r is, according to Little (1969):

$$P_r = \frac{P_t A_r L c \tau \sigma}{2R_s^2} \quad (3.4)$$

Where P_t is the power of the emitted sound, c is the sound speed, R_s is the range to the scattering object, σ is the scattering cross section, τ is the length of the pulse, A_r is the effective aperture area, and L is an attenuation factor. The attenuation factor takes into account the efficiencies of the sound reception and transmission as well as the effects of classical, molecular, and excess attenuation (α_c , α_m , and α_e respectively). The equation was expanded by Neff (1978) such that:

$$L = \alpha_e e^{-2(\alpha_c + \alpha_m)R} \quad (3.5)$$

For the case of a monostatic SODAR, i.e. transmitter and receiver being collocated, Tatarski (1971) (see Kallistratova, 1997 for reference) found the scattering cross section σ to be represented by the following equation:

$$\sigma = 0.0039 \left(\frac{2\pi}{\lambda} \right)^{1/3} \left(\frac{C_T^2}{T^2} \right) \quad (3.6)$$

Where C_T is the temperature structure function parameter and T is the ambient air temperature. The temperature structure parameter and its calculation are detailed in Wyngaard et al. (1971).

Acoustic frequency shift

The principle described above explains the effects of turbulence on the intensity of backscattered acoustic waves. This information does not provide any information regarding the wind speed itself; in fact, wind speed does not directly affect the intensity of the backscatter. Instead, due to the Doppler effect, wind speed results in a shift in frequency of backscattered waves. The SODAR electronics are able to measure the acoustic frequency shift.

When a transmitter emits a pulse while moving towards a receiver, the sound wave is condensed (wavelength shortened) and thus the receiver measures a higher frequency than the emitted frequency. Conversely, if the transmitter is moving away from the receiver, the sound wave is elongated and the receiver measures a lower frequency. The magnitude of the frequency shift related to the speed of the transmitter. For the case of a stationary transmitter and an approaching receiver, the frequency is perceived as increasing because the phase speed relative to the receiver is increased. When the receiver is moving away from the transmitter the frequency is decreased because the relative phase speed is decreased. The relationship between the speed of the transmitter V_r , and the

received frequency, f_s (see Giancoli, 2000, pgs 432-435) is

$$V_r = \frac{c}{2} \left(1 - \frac{f_s}{f_e} \right) \quad (3.7)$$

where f_e is the emitted frequency and c is the speed of sound. In the case of a SODAR system, a pulse is emitted from the SODAR which is then reflected back into the SODAR by turbulent fluctuations. Therefore we can consider the turbulent inhomogeneities to be the transmitter, they scatter the pulse back towards the SODAR at the original frequency modified by the mean wind speed in the direction of the pulse. Thus in the case of a SODAR system, V_r represents the wind speed in the direction of the sound pulse, f_e is the frequency of the emitted pulse, and f_s is the frequency of the backscattered sound.

The monostatic phased array

As mentioned previously, the frequency of a sound pulse is only modified by the mean wind speed *in the direction of that of the pulse*. This means that the real wind vector can be triangulated using a combination of three pulses aimed at different angles. The Metek PCS.2000/MF-24 SODAR used in this experiment was a monostatic system that uses a square shaped array of transceivers. The transceivers are able to adjust the angle of the pulse beams by adjusting the phase of the rows allowing for interference to tilt the phase fronts of the beam. The Metek SODAR is able to send five pulses which will be referred to as antennae $a1$ - $a5$ (see Fig. 3.1) each in a different direction. When the SODAR emits a pulse, the transceiver waits to receive the backscattered signal. The receiving interval is dependent on the length of the pulse, the user defined noise height, and the speed of sound estimated using a ground level measurement of air temperature. The receiving interval is given by the following range:

$$t_m = \left[\frac{2h_{min}}{c}, \frac{2h_{noise}}{c} + \tau \right] \quad (3.8)$$

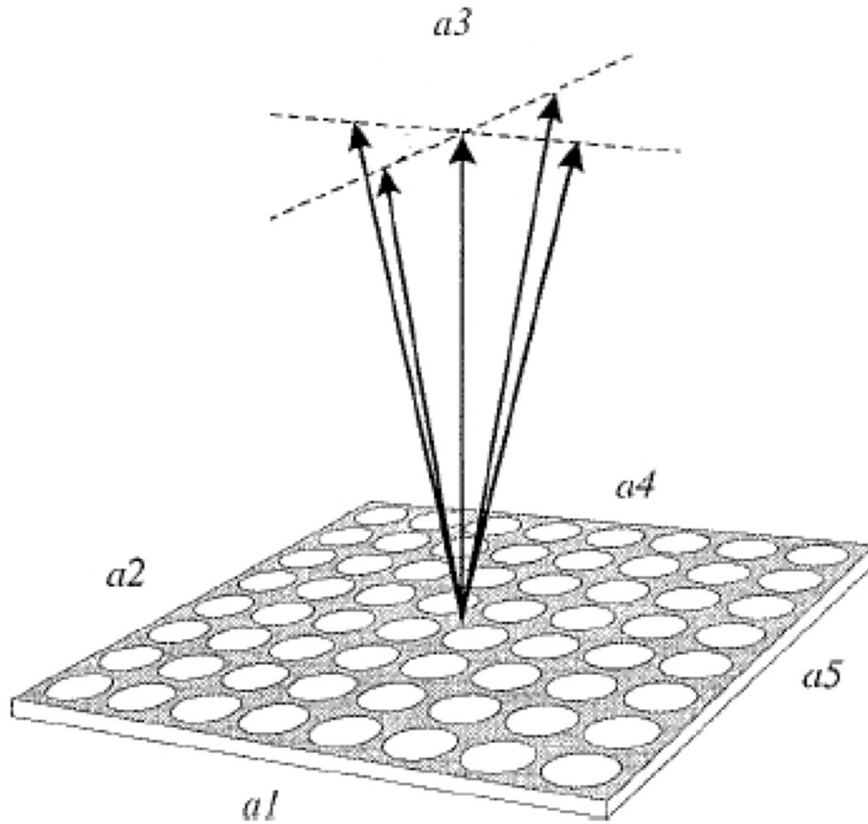


FIGURE 3.1: The square-shaped monostatic phased array. Produces five independent directional pulses $a1 - a5$. Pulse $a3$ is vertical while the others are each separated from $a3$ by a zenith angle ψ . Tilted pulses are separated by their neighbor with a 90° azimuth angle. From: METEK, PCS.2000/MF-24 user manual.

Where h_{min} is the user specified minimum height, h_{noise} is the user specified noise height, c is the speed of sound, and τ is the pulse length. Measurements are made at individual heights by including backscatter received within the following intervals:

$$t_{mn} = \left[\frac{2(h_{min} + n\Delta h)}{c}, \frac{2(h_{min} + n\Delta h)}{c} + \tau \right] \quad (3.9)$$

Where Δh is the user specified height interval and n is gate number in the sequence. The SODAR sends out a pulse with each antenna to complete one sequence saving the

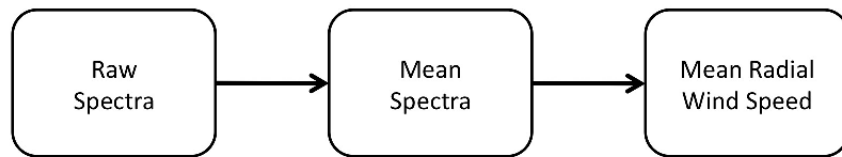
backscattered spectra as raw data. The raw data is then analyzed using the Fast Fourier Transform (*FFT*) (see Appendix A for details on FFT).

3.1.2 Data Processing and Conversion

Before each pulse, the SODAR system takes two independent samples of background noise, performs FFT analysis on them and subtracts the average noise spectra from the main signal spectra. The backscattered signal then undergoes spectral analysis at each SODAR gate separately. The spectra is regressed against a Gaussian shaped distribution (see Appendix A) before being averaged over the user specified averaging interval.

Averaging Modes

The Metek SODAR uses two separate averaging modes, the Spectral Mean method and the Cluster method. Each averaging method has advantages and disadvantages which will be discussed in section 3.3.1. Regardless of which method is used to compute the



(a) Spectral Mean Method



(b) Cluster Method

FIGURE 3.2: Flowchart of the two averaging methods used by the Metek SODAR system. Spectral Mean method uses the mean spectra to calculate radial wind speed whereas cluster averaging takes the median of the pdf constructed from the instantaneous radial wind speed. Spectral mean calculations are detailed in Appendix A

average radial velocities \bar{V}_R , the following equation is always used:

$$\bar{V}_R = c \frac{f_e - \bar{f}_s}{f_e + \bar{f}_s} \quad (3.10)$$

Where f_e is the emitted frequency, \bar{f}_s is the average backscattered frequency, and c is the speed of sound. When using the Spectral Mean method, the backscattered frequency \bar{f}_s is determined from the mean of the spectra taken over the averaging period. When using the cluster method, the f_s values are instantaneous. This means that the V_R values are also instantaneous. The cluster method takes the median of the pdf constructed from the instantaneous V_R values to be the radial velocity for the averaging period. See Figure 3.2 for a flow diagram of the averaging methods.

Additional data output

Because antenna $a3$ is vertical, it allows the horizontal component of each radial velocity \bar{V}_R to be obtained using the following relationship:

$$\begin{aligned} \bar{V}_{H,a} &= \bar{V}_{R,a} - \bar{V}_{R,3} \cos(\psi) \\ \bar{V}_{H,b} &= \bar{V}_{R,b} - \bar{V}_{R,3} \cos(\psi) \end{aligned} \quad (3.11)$$

Where ψ represents the zenith angle of the tilted antennae which is calculated based on the speed of sound, and the subscripts a and b represent a pair of orthogonal antennae (i.e. 1 & 2, 2 & 4, 4 & 5, or 5 & 1). The horizontal radial components $\bar{V}_{H,a\&b}$ can be used to compute the average horizontal wind speed \bar{V} :

$$\bar{V} = \sqrt{\bar{V}_{H,a}^2 + \bar{V}_{H,b}^2} \quad (3.12)$$

When used along with the compass directions of each antenna, α , the horizontal components can be used to calculate the wind direction $\bar{\theta}$:

$$\bar{\theta} = \begin{cases} \arctan \left| \frac{\bar{V}_{H,a}}{\bar{V}_{H,b}} \right| + \alpha_a & \text{if } \bar{V}_{H,a} > 0, \bar{V}_{H,b} > 0 \\ 180 - \arctan \left| \frac{\bar{V}_{H,a}}{\bar{V}_{H,b}} \right| + \alpha_a & \text{if } \bar{V}_{H,a} < 0, \bar{V}_{H,b} > 0 \\ 180 + \arctan \left| \frac{\bar{V}_{H,a}}{\bar{V}_{H,b}} \right| + \alpha_a & \text{if } \bar{V}_{H,a} < 0, \bar{V}_{H,b} < 0 \\ 360 - \arctan \left| \frac{\bar{V}_{H,a}}{\bar{V}_{H,b}} \right| + \alpha_a & \text{if } \bar{V}_{H,a} > 0, \bar{V}_{H,b} < 0 \end{cases} \quad (3.13)$$

Cartesian velocity components \bar{u} , \bar{v} and \bar{w} can then be computed as follows:

$$\bar{u} = \bar{V} \cos(\bar{\theta}) \quad (3.14)$$

$$\bar{v} = \bar{V} \sin(\bar{\theta}) \quad (3.15)$$

$$\bar{w} = -\bar{V}_{R,3} \quad (3.16)$$

For the purposes of this experiment, the directional convention is that \bar{u} is positive towards the east, and \bar{v} is positive towards the north. In addition to velocity values, the Metek software also provides standard deviations, reflectivity, and error codes for each radial antenna. The error codes and their explanations can be seen in Appendix B.

3.1.3 Limitations to the SODAR technique

The use of SODAR is predominantly limited by factors that result in the attenuation of the SODAR beam. The primary sources of sound attenuation (see Eq. 3.5) are classical attenuation α_c , molecular attenuation α_m , and excess attenuation α_e . Classical attenuation occurs due to viscosity, heat conduction, and molecular diffusion and is well understood. The effects of classical attenuation are minimal in comparison with the molec-

ular attenuation at frequencies used by the SODAR (Neff, 1975). Molecular attenuation occurs due to excitation of O_2 molecules with the passing of acoustic waves (Neff, 1978). The effects of molecular attenuation increase linearly with increasing frequency and also vary inversely with relative humidity (Harris, 1966). Figure 3.3 shows the relationship be-

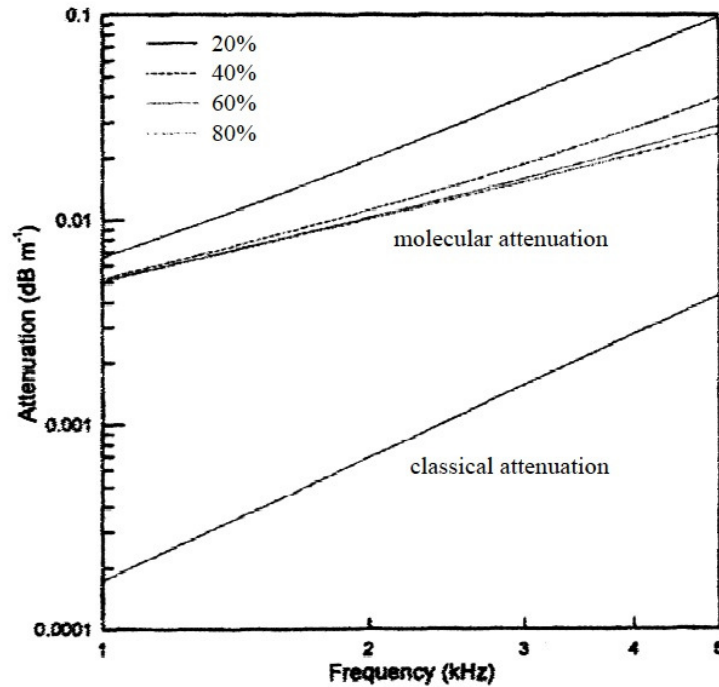


FIGURE 3.3: Illustration of classical and molecular attenuation as a function of sounding frequency (equations come from Neff (1975)). The varying percentages in the upper left corner correspond to relative humidity and the plot shows how molecular attenuation varies inversely with humidity (Crescenti, 1998).

tween classical and molecular attenuation, and sounding frequency. The effects of excess attenuation are smaller than those of the other two contributors but can not be neglected as they have shown themselves to increase rapidly with height (Moulsley et al., 1979).

SODAR signals are highly sensitive to environmental noise. In general, it is best to limit the noise exposure of a SODAR system to minimize the risk of limiting the

availability of good velocity data. A detailed description of how noise is separated from the SODAR signal is presented in Appendix A. Background noise is usually characterized as active, broadband noise. Broadband, as opposed to narrow-band, covers a large range of frequencies and poses a severe problem for SODAR measurements as it can overlap the sounding frequency and reduce the Signal Noise ratio (S/N). As the SODAR signal intensity decays with height eventually the S/N decreases below acceptable levels and the data is discarded. Narrow-band noise typically includes intermittent sources such as birds or insects. These types of noise only present a problem when their frequencies overlap with the sounding frequency. However, if they do overlap, narrow band noise sources can result in false wind measurements that are difficult to identify when the noise is persistent. During periods of weak turbulence, the overall acoustic reflectivity (i.e. intensity of backscatter) is slightly decreased. This results in increases to both acoustic attenuation and noise sensitivity. Therefore the maximum gate height is reduced during periods of weak turbulence e.g. nocturnal conditions.

An additional limitation of a SODAR system is interference from passive noise sources. Passive noise sources are stationary objects that reflect part of the SODAR beam back into the transceivers. When this occurs, the signal registers a constant zero value for the Doppler shift because the object is not moving. These effects are called fixed echos. It is important for antennae to be aimed away from tall objects such as trees, towers, buildings, etc.. Fixed echoes and sources of periodic narrow-band noise are things that can be difficult to foresee when installing a SODAR. Consequently, SODAR data needs to be checked shortly after installation in order to identify any potential sources of interference and to adjust the orientation of the antenna array if necessary.

3.2. DONUTSS-2010 Field Experiment

All of the data used in this research were collected during the Direct Observation of Near-surface Turbulent and Sub-meso Structures 2010 experiment (DONUTSS-2010). DONUTSS-2010 was conducted at the Oregon State University (OSU) Biology and Plant Pathology (BPP) site in Corvallis, Oregon, USA ($44^{\circ} 34' 1''$ N, $123^{\circ} 14' 32''$ W) from June until November 2010. With an elevation of $65.5 \text{ m} \pm 1.5 \text{ m}$ above sea level and sparse canopies ranging from 1 m to 4 m above ground level (agl), the site was chosen for its moderate surface heterogeneity as well as its proximity to OSU campus facilities and line power.

3.2.1 Site Layout

The DONUTSS-2010 experiment included the use of multiple SODAR sites and a pair of Metek PCS.2000/MF-24 SODAR systems which were designated *S* and *R*. One of these systems was kept stationary (*S*) at the core site along with the rest of the sensors used during the experiment (Thomas et al., 2012), while the other was a roving (*R*) system. The second SODAR was sequentially moved from one location to another spending a period of ≈ 10 days at each site. Figure 3.4 shows a map of the local area including a diagram of the location of each SODAR site.

BPP site

The core site, seen in Figure 3.4 as the southernmost location, consisted of the largest concentration of sensing equipment. The stationary SODAR was located about 15 meters to the southwest of a 7 meter tower which anchored a pair of Metek USA-1 sonic anemometers. The anemometers were located at 7.0 meters and 1.6 meters agl.

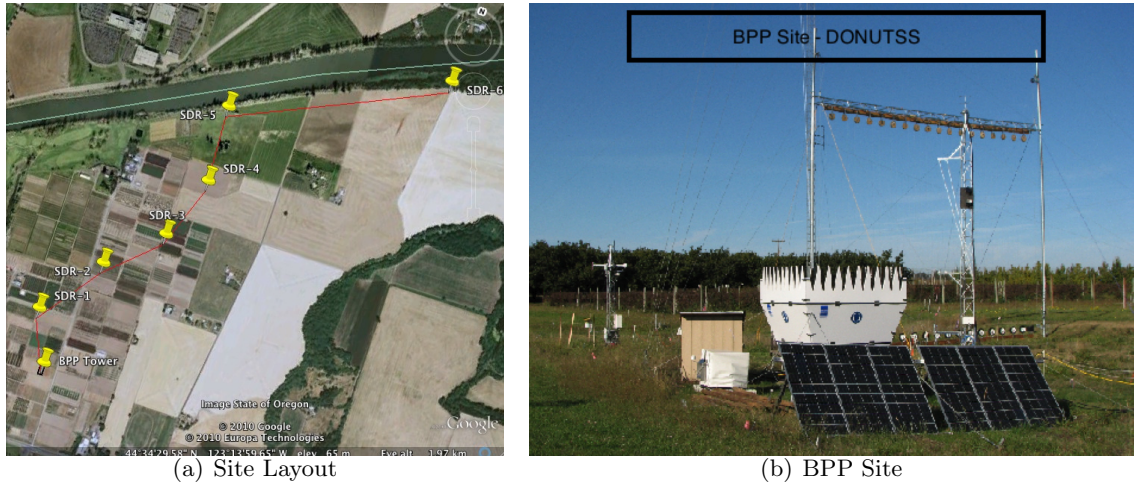


FIGURE 3.4: (3.4(a)) SODAR migration pattern, note that the BPP Tower marked in the image is actually the core BPP site. (3.4(b)) Deployed SODAR with BPP tower and DTS Harp unit shown in the background.

Roving SODAR sites

The deployment sequence of the moving SODAR is illustrated in Figure 3.4. Details of each site are shown in Table 3.1. The first four R locations were large clearings free of obstacles. While the last two locations were also clearings, the north end of those clearings were lined with trees which exceeded 20 meters in height.

TABLE 3.1: Table showing site locations for each SODAR location used during the DONUTSS-2010 experiment. Includes information regarding the separation distance between each R site and the S site.

Site	Latitude	Longitude	Duration	Distance from core site
BPP Site	44° 34' 1" N	123° 14' 32" W	07/06- 10/25	0 m
SDR-1	44° 34' 8" N	123° 14' 36" W	07/12 - 07/26	241 m
SDR-2	44° 34' 17" N	123° 14' 26" W	07/26 - 08/12	511 m
SDR-3	44° 34' 23" N	123° 14' 16" W	08/12 - 08/27	779 m
SDR-4	44° 34' 33" N	123° 14' 12" W	08/27 - 09/13	1078 m
SDR-5	44° 34' 44" N	123° 14' 12" W	09/13 - 10/14	1390 m
SDR-6	44° 34' 57" N	123° 13' 32" W	10/15 - 10/25	1735 m

3.2.2 SODAR Setup and User Settings

When deploying a SODAR system, there are a number of factors to consider. The first item to consider is site selection and preparation. Referring back to section 3.1.3, it is important to select a site that has limited noise sources. Keeping the SODAR a sufficient distance from roads and tall obstacles can limit the influence of active broadband and passive noise sources. Once the site is selected, the next step is deploying the SODAR. The systems used here were equipped with the following items:

- Metek PCS.2000/MF-24 Phased array of 24 loud speakers
- Layer of sound shielding
- SODAR electronics with PC interface
- Photovoltaic array and 24 VDC battery bank

The first step when setting up a SODAR system is to ensure that the top of the antenna is exactly level. This ensures that antenna $a3$ measures exactly the vertical wind component. The next step is to measure the azimuth α_1 of antenna $a1$ using a compass. The Metek PC user interface provided with the SODAR allows for easy adjustment of measurement parameters. Once α_1 is entered into the user interface, the rest of the antenna azimuths are automatically adjusted according to the following relationship:

$$\alpha_2 = \alpha_1 + 90$$

$$\alpha_4 = \alpha_1 + 180$$

$$\alpha_5 = \alpha_1 + 270$$

Construction of the acoustic shielding needs to be performed carefully as to avoid moving the array. It is also important to keep the shield an equal distance from all sides of the array to ensure that the signal is free of directional bias. The Metek SODAR allows for

multiple sounding frequencies to be used simultaneously. The following user specifications were made to the SODAR controls before operation.

- Sounding frequencies (f_e): 1.7, 2.1, 2.5, & 2.9 kHz
- Averaging mode: Mean spectra & Cluster methods (both)
- Minimum gate height (h_{min}): 15 m
- Height step interval (Δh): 10 m
- Maximum gate height (h_{max}): 295 m
- Noise height (h_{noise}): 325 m
- Averaging length (t_{ave}): 2 min

3.2.3 Checking for fixed echoes

Before allowing a SODAR system to run operationally, it is important that the data be checked for the influence of passive noise. As mentioned in Section 3.1.3, passive noise sources cause fixed echoes. A fixed echo will cause data to show a constant zero wind speed. In order to identify fixed-echoes in the data, one must observe the reflectivity time series output by the SODAR. A fixed echo will result in a band of increased reflectivity that occurs regardless of meteorological conditions. In order to find these, a continuous data set comprised of both day and night conditions must be observed. Fixed echoes can be located by plotting the reflectivity in the form of a color plot, commonly referred to as a sodargram (see Figure 3.5). These echoes can occur even in the absence of tall obstacles. This is due to side-lobes of the antenna beams which are known to increase in size with decreasing frequency (Crescenti, 1998). Once detected it is sometimes possible to eliminate fixed echoes by rotating the antenna beams away from passive noise sources or relocating the antenna slightly.

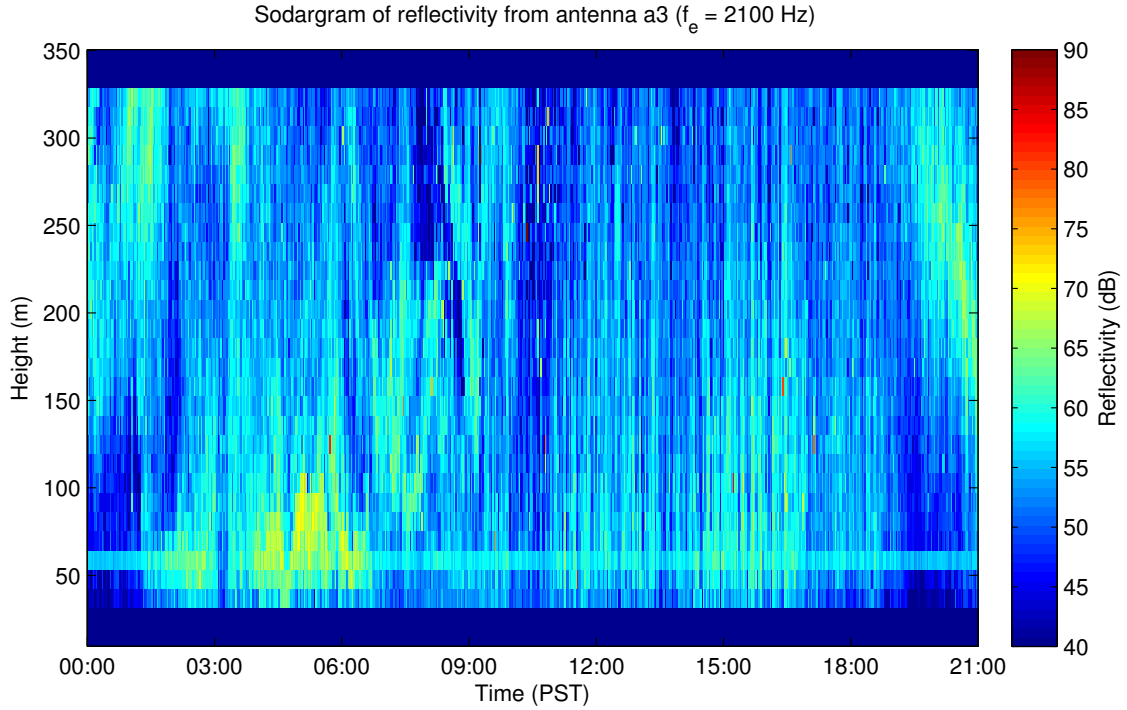


FIGURE 3.5: Example of a fixed echo taken from the DONUTSS-2010 field experiment (Date: June 20th 2010, 00:00 to 23:58 PST). The echo is indicated by a band of constant reflectivity located a 55 m agl.

3.3. Data Quality Control

SODAR data taken from the experiment was archived into daily ASCII files and imported into MatLab format using a customized data processing script written in MatLab. Sonic data sampled at 10 Hz was archived into hourly files and aggregated into 2 minute averages and added to the SODAR data set. Before performing any analyses, the SODAR data needed to be optimized.

3.3.1 Selecting SODAR averaging method

The Metek PCS.2000/MF-24 SODAR system has a recommended averaging time of 10 minutes to 30 minutes in order to ensure the maximum signal quality. For the purpose

of this study, the SODAR averaging time was set at 2 minutes thus ensuring the maximum temporal resolution allowed by the SODAR. Due to the unusually small averaging time of this study, there occurred a noticeable increase in error code occurrences throughout the SODAR data (see Figure 3.6). In order to select the ideal averaging method, spectral mean or cluster, some analysis needed to be performed. The distribution of the vertical

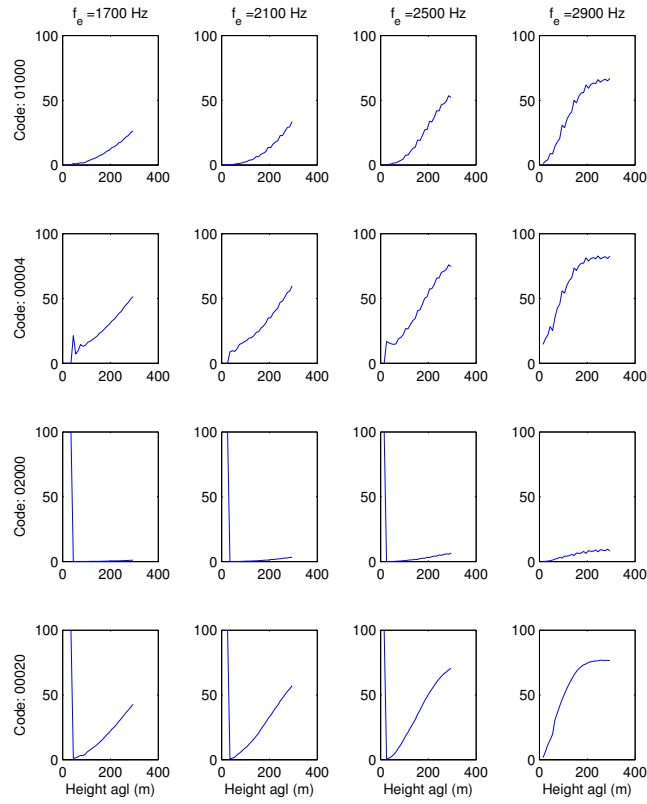
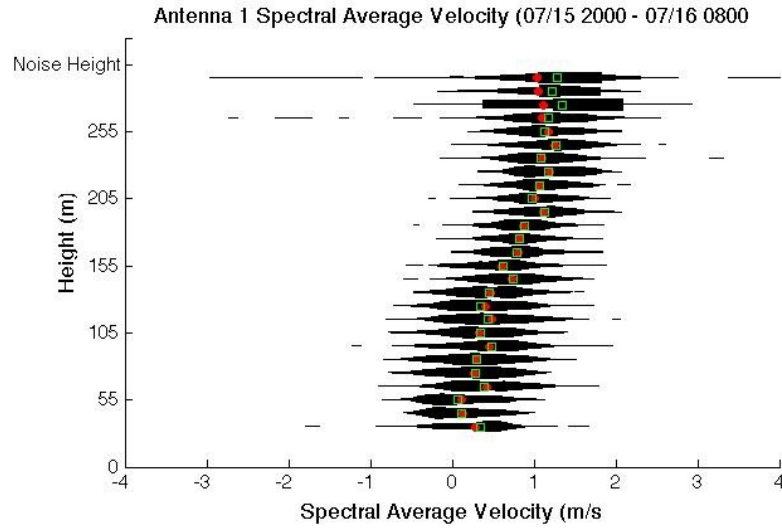
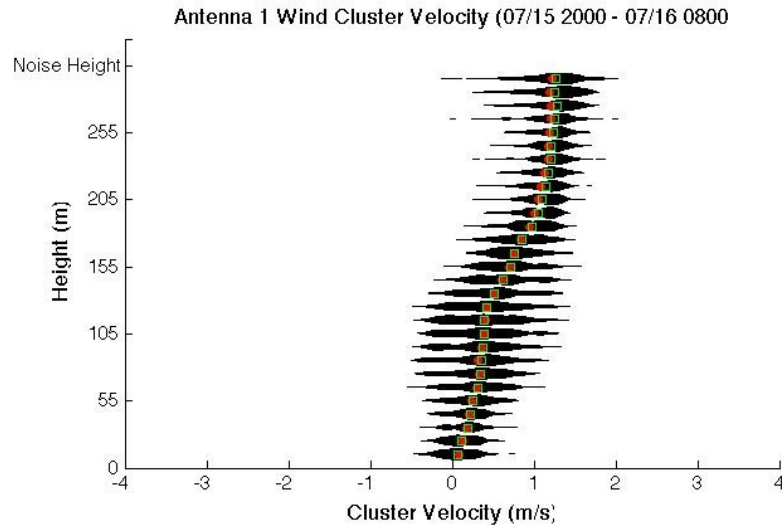


FIGURE 3.6: The percentage of data from antenna *a1* affected by each type of error code as a function of height. The error percentages are calculated for each sounding frequency and represent the entire data record. Notice increases in codes 01000, 00020, and 00004. See Table 0.1 for explanation of error codes.

wind profile taken by the SODAR during a relatively calm period can be seen in Figure 3.7. The figure shows distribution plots of horizontal wind speed values taken using both the mean spectra (3.7a) and the cluster (3.7b) technique.



(a) Mean spectra



(b) Cluster

FIGURE 3.7: (3.7(a)) PDF of west-east velocity distribution at each SODAR gate height taken using the mean spectra method. (3.7(b)) PDF of west-east velocity distribution at each SODAR gate height taken using the cluster method.

The distribution of wind speed taken using the spectral averaging method shows a significantly higher standard deviation. This could be a result of that methods sensitivity to outliers in the spectra. The existence of spectral outliers in a small data set causes severe overestimation of the mean. Due to the severe deviation of data collected using the spectral mean technique, the remainder of this research was conducted using data collected using the cluster technique.

3.3.2 Selecting SODAR sounding frequency

Due to relationship between acoustic attenuation and the sounding frequency (see Section 3.1.3) it was important to optimize the selected frequency. Since the Metek SODAR system is capable of sampling at multiple sounding frequencies simultaneously, we were able to optimize the frequency after data collection. As mentioned in Section 3.1.3, classical and molecular attenuation is known to increase linearly with sounding frequency thus limiting the maximum gate height. This effect is verified by observing the effect of sounding frequency on the percentage of data affected by certain error codes (See Figure 3.6). While maintaining the maximum height range is important, it is also important to avoid increasing the width of the antenna beam by reducing the frequency too low. Reducing the frequency also increases the size of antenna side-lobes thus increasing the influence of passive noise (Crescenti, 1998). A sounding frequency of 2.1 kHz was selected for the remainder of this research as it strikes a balance between data quality, availability and beam width.

3.3.3 Azimuth Corrections

The final step in quality control was ensuring that all antenna beams were assigned the correct azimuth. Any systematic difference in wind direction can significantly affect correlation statistics between measurement sites so proper alignment is important. It was possible to align and correct for azimuth offsets by assuming that, at high elevations

(<150 meters agl) under high wind conditions, wind direction measurements between SODAR systems would agree. The use of data sampled at upper SODAR gates eliminates the influence of surface drag of wind direction and strong winds tend to have reduced directional variability. Under this assumption, by plotting the difference between the stationary SODAR $\bar{\theta}$ at upper elvations and the moving SODAR $\bar{\theta}$ at the same elevation against \bar{V} the direction difference could be determined. The equation below illustrates the technique:

$$\lim_{\bar{V}(t) \rightarrow +\infty} (\bar{\theta}_S(t) - \bar{\theta}_R(t)) = (\alpha_S - \alpha_R) \quad (3.17)$$

Azimuth corrections were applied to the moving SODAR sites in post-processing such that the limit shown above would equal zero (See Table 3.2).

TABLE 3.2: SODAR azimuth corrections for each Roving SODAR location. Corrections are made to the Roving SODAR system relative to the azimuth of the Stationary SODAR system.

Site	α_R correction
SDR-1	+30°
SDR-2	+28°
SDR-3	+15.5°
SDR-4	+34°
SDR-5	+19°
SDR-6	+7°

4. DATA ANALYSIS TECHNIQUES

This chapter will cover all of the analysis techniques used to investigate the variability of near surface winds under weak conditions. First a technique used to investigate turbulent processes on multiple time scales will be discussed. Then the chapter will cover the bulk statistics used to make comparison between different elevations and horizontal locations.

4.1. Multi-Resolution Decomposition

This study requires that wind data be observed on a variety of time scales. In order to accomplish this, it will make use of the Multi-Resolution Decomposition (MRD) technique. This method, based on the Haar transform, is naturally suited to turbulent flux observations (Howell and Mahrt, 1997, Katul and Parlange, 1995, Mahrt and Howell, 1994, Shore, 1973). MRD is essentially a moving block average of a time series performed at multiple time scales simultaneously. There are four advantages that the MRD technique has over the more common Fourier analyses:

- Fourier cospectra are dependent on the periodicity of turbulent events, including the periodicity of the time between these events. Turbulence is generally non-periodic which makes the interpretation of peaks in the Fourier cospectra ambiguous. MRD, on the other hand, decomposes covariances locally so the averaging length depends not on the periodicity of the event, but rather on the length of the dominant event.
- The MRD method obeys Reynolds averaging by using non-overlapping moving averages. In the case of Fourier decomposition, the use of weighted averages causes mean perturbation terms not to vanish (i.e., $\overline{u'v} \neq 0$) (Howell and Mahrt, 1997).

- The MRD technique uses an algorithm based on the Fast Haar Transform (FHT) which requires on the order of N arithmetic operations. This makes it less computationally expensive than the FFT which requires on the order of $N \log N$ operations (Beylkin et al., 1991).
- While Fourier provides a single coefficient for each wavelength, the local nature of the MRD technique allows for the calculation of a sample variance for a cospectrum value at each time averaging scale (Howell and Mahrt, 1997).

4.1.1 MRD Averaging Scheme

Thinking of the MRD technique as a series of moving block averages is a simple way of linking it to Reynolds averaging (Howell and Mahrt, 1997). Consider a time series of size N , in order for orthogonal MRD to work N must equal some value 2^M where M is any integer. Letting each value of this time series be represented as w_i , we can show mathematical definition of each average value \bar{w}_n that is output by the MRD where n is the window number.

$$\bar{w}_n(2^m) = \frac{1}{2^m} \sum_{i=(n-1)2^m}^{n2^m-1} w_i \quad (4.1)$$

Where m is any integer falling between 0 and M corresponding to an averaging interval of size 2^m . If there is another variable ϕ which varies along with w , a flux can be computed,

$$w'_i(2^m)\phi'_i(2^m) = [w_i - \bar{w}_n(2^m)] [\phi_i - \bar{\phi}_n(2^m)] \quad (4.2)$$

Where $\bar{\phi}_n$ is computed using equation 4.1. This result can be used to compute the flux within each individual averaging window:

$$w'_n(2^m)\phi'_n(2^m) = \frac{1}{2^m} \sum_{i=(n-1)2^m}^{n2^m-1} w'_i(2^m)\phi'_i(2^m) \quad (4.3)$$

Table 4.1 displays MRD output for an N value of 64 and a time series w that consists of 2 minute averages. Figure 4.1 shows a graphical interpretation of the MRD process.

TABLE 4.1: This table applies to a 64 point data set with each point representing a 2 minute sample average. The table shows the size of each averaging interval and the number of averaging intervals possible when an MRD routine is applied to the data set.

Mode	Averaging length	# of windows
0	2 min	64
1	4 min	32
2	8 min	16
3	16 min	8
4	32 min	4
5	64 min	2
6	128 min	1

4.1.2 Modifications

The orthogonal MRD requires that there be no overlap between averaging windows. However, when working with real time series it is very unlikely that the size of a data set will be exactly a power of 2. In order to accommodate a data set of arbitrary size N , we fabricate a new time series with 2^M points, such that $2^{M-1} < N \leq 2^M$. The new time series can be considered to represent the same period of time as the original time series but with a finer resolution. The points on the new time series are then filled in by interpolating between points on the original time series. The new time series will have a new interval:

$$t'_{ave} = t_{ave} \frac{N - 1}{2^M - 1} \quad (4.4)$$

4.1.3 Implementation

For this research, the data set that would be processed using MRD required pre-processing. The data was first divided into a set of sequential 64 minute periods. These

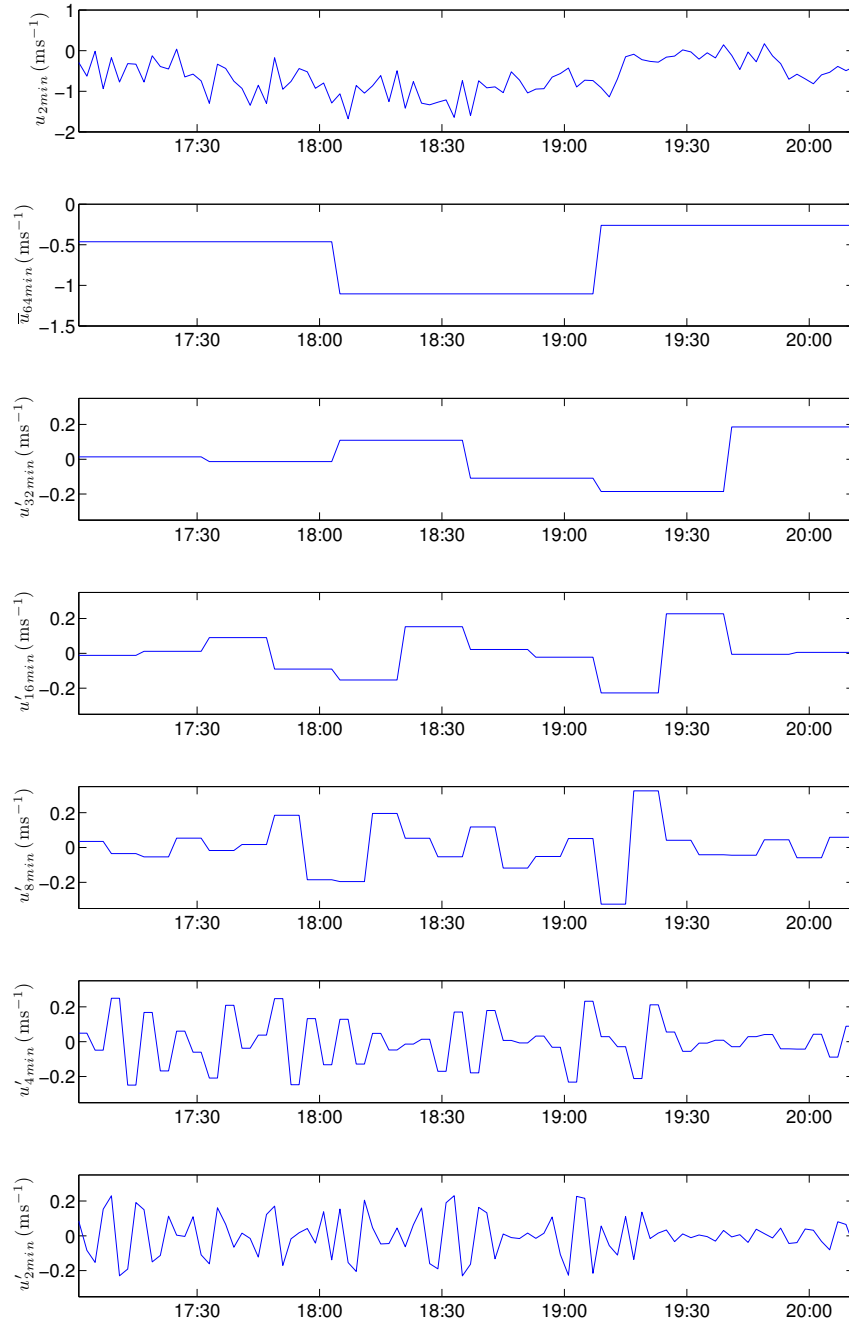


FIGURE 4.1: A graphical representation of the MRD process. The raw time series in this case is shown in the top plot. The second plot shows the 64 minute mean values, and subsequent plots show the perturbation values for time scales of 32 and 16 minutes.

periods were designed to begin on the hour. This meant that each 64 minute time series would overlap the subsequent time series by 4 minutes. In order to ensure that the time-series being decomposed using MRD was continuous, data were gap filled using a "nearest value" gap filling scheme. The pre-processing routines allowed for a gap of up to 20 missing values to be filled. Each 64 minute period was then processed with MRD individually.

4.2. Post MRD filtering

Gap filling performed on missing values before MRD processing can cause problems when computing bulk statistics for station comparisons. Therefore, in order to limit bias due to gap filling effects, only 64 minute intervals containing fewer than 2 gap filled values were included in the analyses. As mentioned previously, reduced signal intensity with increased SODAR gate height reduces the S/N ratio at upper heights. When the S/N ratio decreases below a certain point, the SODAR produces an error code (See Table 0.1) and the data corresponding to that height level is discarded. This means that the number of gap filled values increases with increasing gate height. The reduction of data availability with height is summarized in Figure 4.2. Since gapfilling reduces the statistical significance of the data, only profiles containing minimal gaps were analyzed. By reducing the height range of profiles to be analyzed, the number of gap free profiles is increased.

4.3. Bulk Statistics

In order to visualize a data set of this size, bulk statistics were employed. The primary statistic used here was the bulk temporal correlation coefficient, $R_{xy,m}$ calculated

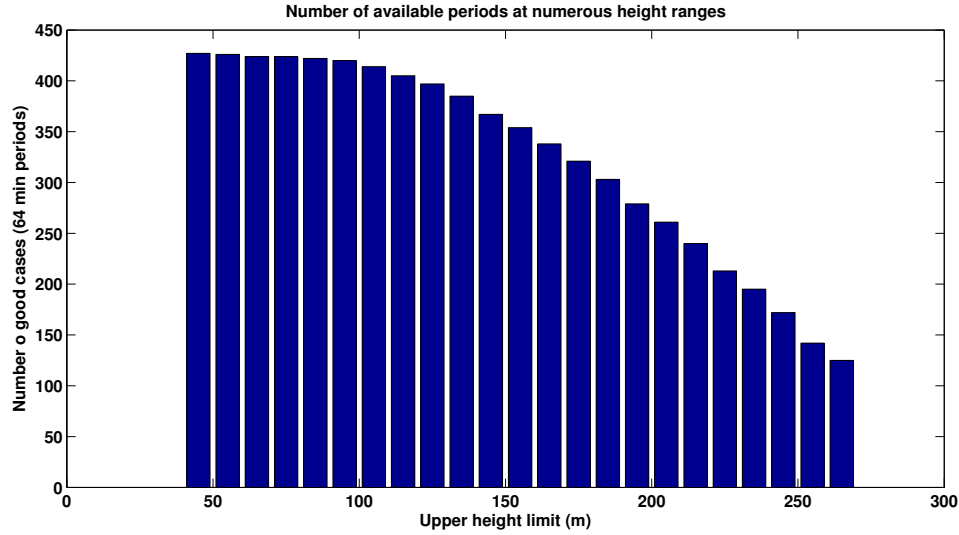


FIGURE 4.2: Chart showing the number of 64 minute periods containing no missing values. Only 64 minute periods containing fewer than 2 gap filled values across all stations were used to compute correlation statistics. The maximum height chosen for correlation statistics was 155 meters thus preserving approximately 80% of the data.

using the autocorrelation function:

$$R_{xy,m} = \frac{\sum_{t=1}^T (x_m(t) - \bar{x})(y_m(t) - \bar{y})}{\sqrt{\sum_{t=1}^T (x_m(t) - \bar{x})^2} \sqrt{\sum_{t=1}^T (y_m(t) - \bar{y})^2}} \quad (4.5)$$

Where the x and y can be any variable, and the subscript m indicates the MRD mode. Correlations between SODAR stations were made by computing the correlation coefficients for each directional wind component u and v then combining the coefficients. The

equations used to accomplish this are shown below:

$$R_{u_S, u_{R,m}} = \frac{\sum_{t=1}^T (u_{S,m}(t) - \overline{u_S})(u_{R,m}(t) - \overline{u_R})}{\sqrt{\sum_{t=1}^T (u_{S,m}(t) - \overline{u_S})^2} \sqrt{\sum_{t=1}^T (u_{R,m}(t) - \overline{u_R})^2}} \quad (4.6)$$

$$R_{v_S, v_{R,m}} = \frac{\sum_{t=1}^T (v_{S,m}(t) - \overline{v_S})(v_{R,m}(t) - \overline{v_R})}{\sqrt{\sum_{t=1}^T (v_{S,m}(t) - \overline{v_S})^2} \sqrt{\sum_{t=1}^T (v_{R,m}(t) - \overline{v_R})^2}} \quad (4.7)$$

$$R_{S,R,m} = \sqrt{\frac{R_{u_S, u_{R,m}}^2 + R_{v_S, v_{R,m}}^2}{2}} \quad (4.8)$$

The subscripts S and R used here represent the stationary and roving SODARs, respectively. The procedure shown above is comparing wind speed measurements made between the stationary and roaming SODARs. A modified procedure was used to compare measurements made at the lowest SODAR gate height and measurements made at each gate height above it. Note that dividing by the squared root of 2 is simply meant to normalize the correlation coefficient such that it falls between 0 and 1.

5. RESULTS & DISCUSSION

5.1. Near surface flow characterization

Because the goal of this project was to characterize *near surface* motions and their behavior under conditions of weak wind, steps were taken to isolate the weak flows from the strong flows. This would create two separate flow regimes for comparison, the strong regime and the weak regime.

5.1.1 Definition of flow regimes

Figure 5.1 illustrates the relationship between mean wind speed and directional variability near the surface. The figure provides difference in wind direction between heights of 7 meters and 1.6 meters agl as a function of the mean wind speed measured by the 7 meter sonic anemometer. The results reinforce the use of the term "light and variable" as the wind direction variability between heights is dramatically increased under weak winds. Based on the results shown in Figure 5.1 a critical mean wind speed threshold of 1.5 ms^{-1} , measured by the 7 m sonic, was selected. This wind speed threshold accounts for 90% of the variability thus isolating instances of high directional variability. In the interest of including continuous periods of high wind variability, data were filtered based on the 64 minute mean wind speed at the 7 meter sonic rather than by 2 minute values. Filtering the data caused the record to be divided into a pair of exclusive data sets, one representing weak surface winds and the other representing strong surface winds. The separation of the flow regimes allows for the comparison of the mean profiles and bulk statistics based on mean wind speed as well as the location of weak wind cases for the purpose of a case study. The number of 64 minute periods for each new data set at each horizontal configuration is summarized in Table 5.1.

The effectiveness of the 64 minute, critical wind filtering technique are illustrated in

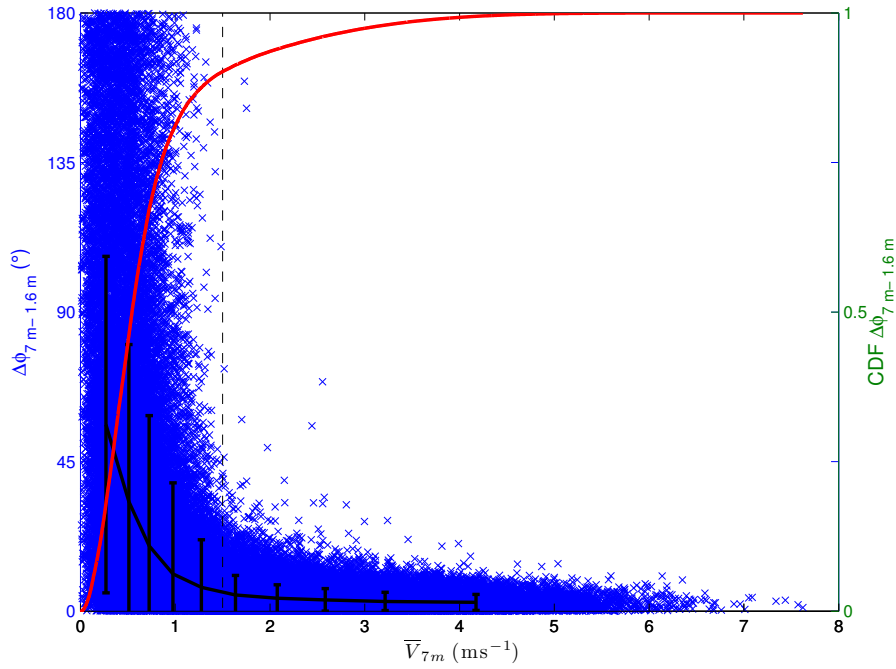


FIGURE 5.1: Difference in sonic direction measurement between upper and lower sonics as a function of horizontal velocity at upper sonic. The dotted line indicates location of critical wind speed (1.5 ms^{-1}). Error bars are shown with the black solid lines and the cumulative distribution of the directional difference is given by the red line.

Figure 5.2. The inclusion of values exceeding the critical wind speed in each regime is the result of filtering by 64 minute average, some of the instances within each 64 minute period exceed the critical wind speed. The strong wind regime shows relatively small directional differences between the sonics with very low deviation. Conversely, the weak wind regime shows extreme differences in wind direction between the sonics, some of which approach 180° confirming the findings of Mahrt (2008b).

5.1.2 Mean profiles for flow regimes

Based on Figure 4.2 a maximum gate height of 155 meters was selected thus preserving approximately 80% of the total available periods. The profiles shown in Figure 5.3 represent the mean velocity profiles for each SODAR separation distance and for each flow regime. Comparing the wind speed and direction profiles between the roving and the

TABLE 5.1: Results of the critical wind filter being set at 1.5 ms^{-1} at 7 meters in terms of the number of 64 minute periods available for each data set up to a level of 155 meters.

Date	Sep. Distance	N for $\leq 1.5 \text{ ms}^{-1}$	N for $> 1.5 \text{ ms}^{-1}$
07/12 - 07/26	241 m	39	22
07/26 - 08/12	511 m	87	41
08/12 - 08/27	779 m	78	25
08/27 - 09/13	1078 m	98	27
09/13 - 10/14	1390 m	162	51
10/15 - 10/25	1735 m	40	7
Total		504 weak winds	173 strong winds

stationary SODAR stations yields a good agreement between the two instruments in all cases with the exception of the final configuration. The disparity between the measurements made during the final phase could possibly be explained by local circulation effects due to the roving SODAR station's close proximity to the row of trees and the river to its north (see Figure 3.4a). The horizontal wind speed profiles show strong winds aloft (above 80 m agl) in each flow regime. However, below 80 m agl the weak wind regime shows a general decrease in horizontal wind speed whereas the profiles in the strong wind regime tend to maintain relatively high wind speeds. The wind direction profiles for each SODAR separation distance, the average wind directions are slightly different. A notable comparison of the direction profiles between wind speed regimes can be made within the lowest 65 meters. The profiles within the strong wind regime show limited variability with height while the profiles within the weak wind regime show a strong rotation of the wind vector centered around 35 m agl. Beginning at 15 meters, the weak regime wind vectors appear to gradually rotate westward with height. The westward component peaks at 35 m agl at which point the vectors begin rotating eastward with height until 65 m agl at which point the vectors maintain their orientation with height. This effect seems to be systematic as it does not appear in the strong wind speed regime and is consistent across all configurations.

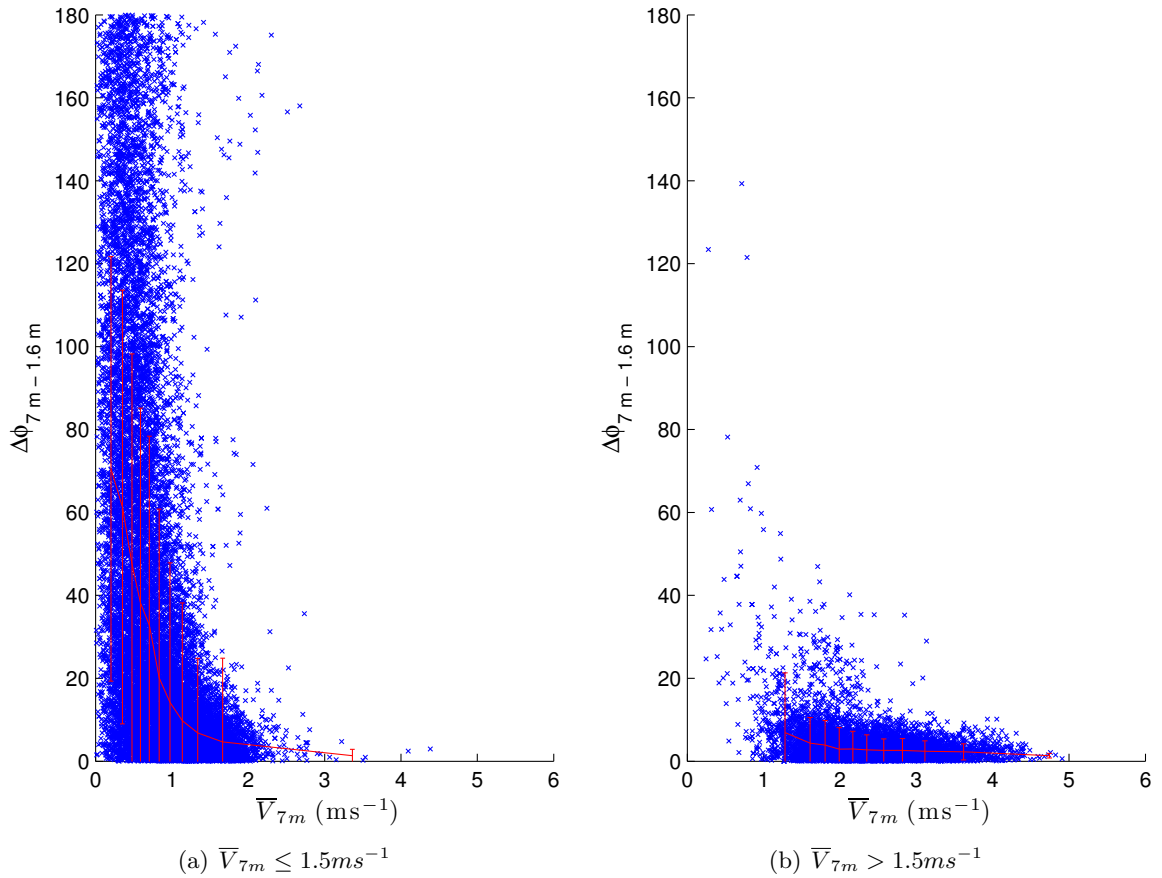


FIGURE 5.2: The plots show the effect of filtering by 1.5 ms^{-1} at 7 meters on the directional variability between the two sonics. Red lines indicate the mean and standard deviations of each bin. Filtering was performed on 64 minute periods based on the mean wind speed of each period. This plot shows all of the 2 minute values contained within those periods. Thus some values exceed the critical wind speed despite the filtering.

5.1.3 Observation of directional variability as a function of upper level wind shear

The weak-wind regime profiles in Figure 5.3 provide evidence of a relationship between the mean vertical wind shear aloft and the direction of the mean wind within the lowest 65 meters of the boundary layer. In order to investigate this relationship, the vertical shear was calculated for each SODAR separation between the gate heights of 55 m agl and 115 m agl. These values were then compared to the directional difference between gate heights 35 m agl and 25 m agl for each SODAR separation. The results of these

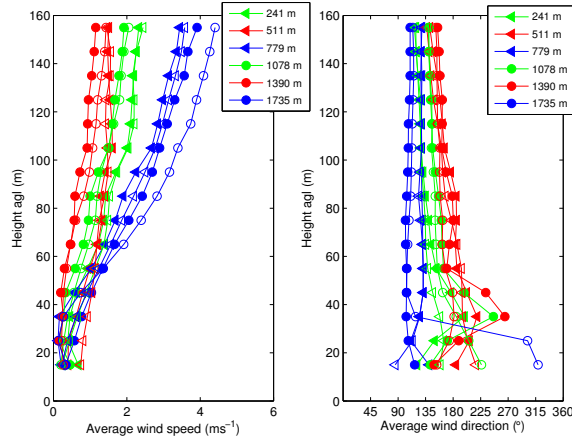
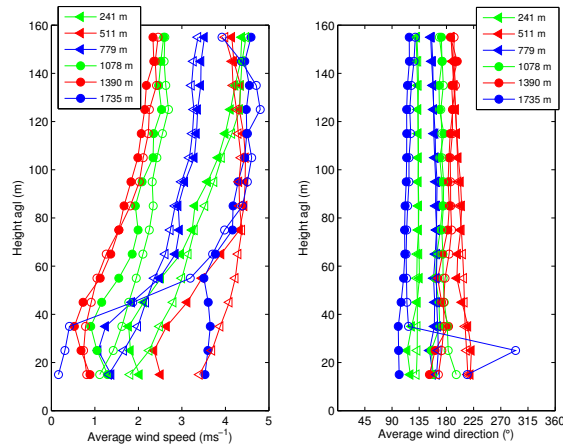
(a) $\bar{V}_{7m} \leq 1.5 \text{ m s}^{-1}$ (b) $\bar{V}_{7m} > 1.5 \text{ m s}^{-1}$

FIGURE 5.3: The mean horizontal wind speed (right) and the mean wind direction (left) for each station, gate height, and SODAR separation distance. Horizontal separation distances between the SODARs measured in meters are indicated in the legend. Solid markers indicate the stationary SODAR and open markers indicate the roving SODAR.

comparisons are illustrated in Figure 5.4. The regression line in Figure 5.4 shows the observed relationship between vertical speed gradient and directional shear between 25 and 35 meters. It was necessary to observe this phenomenon on shorter time scales and attempt to see what was unique about the configurations in which these cases occurred. Observations of each SODAR configuration at a 32 minute time scale (see Figure 5.5) show a high degree of variability. The short time scale observations do not reflect the

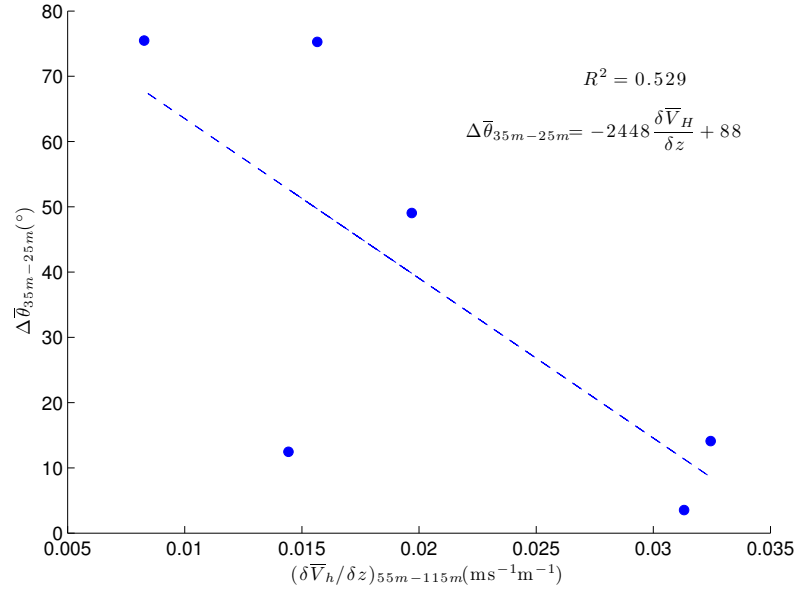


FIGURE 5.4: Plot of the relationship between the wind variation at the lowest gate heights and the velocity shear at the upper gate heights. Points are averaged over the periods contained within each horizontal SODAR configuration. The regression line accounts for approximately 53% of the variability.

relationship between upper level shear and low level flow variability that is illustrated in Figure 5.4. Observations made between the upper and lower sonic measurements yield similar results showing no significant relationship between directional variability and upper level shear (see Figure 5.6). These results imply that wind speed and upper level shear are not the only factors affecting flow variability near the surface. It is likely that stability (static and dynamic) also plays a role in the susceptibility of near surface flows to external forcing.

5.2. Bulk statistics

This section describes the results of three different forms of correlation analysis. The correlation statistics used in the analysis are covered in Section 4.3..

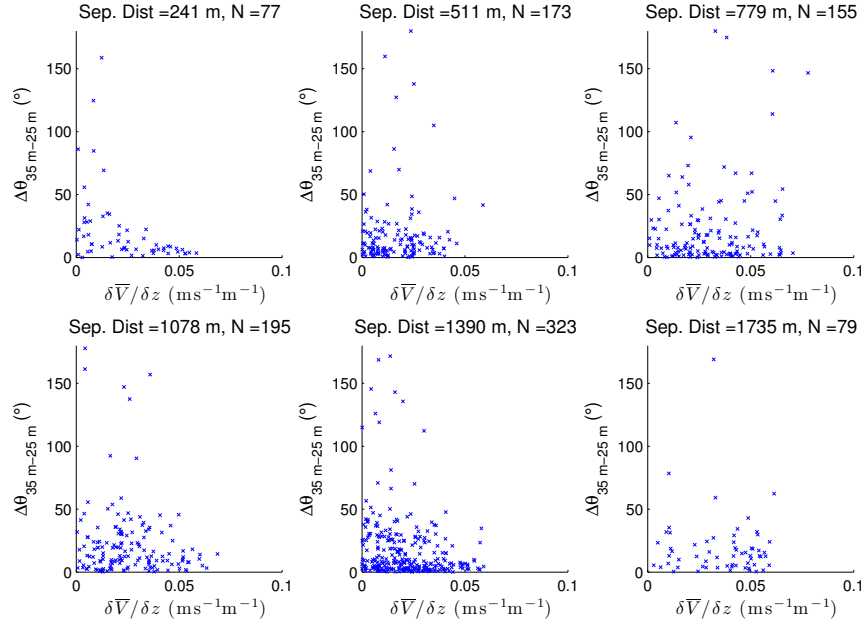


FIGURE 5.5: Wind direction difference between the 35 m agl and 25 m agl SODAR heights plotted as a function of wind shear computed between heights 55 m agl and 115 m agl. Each data point represents a 32 minute average.

5.2.1 Vertical Correlations Between Gates

The following analysis was performed in order to explain the behavior of atmospheric structures as a function of vertical extent, time scale, and flow regime. As described in Section 3.1.1 a gate represents the vertical height range over which the SODAR averages the received spectrum to determine the Doppler shift and the resulting wind speed. Figure 5.7 shows correlation statistics comparing wind velocity at each gate (up to 155 m agl) to the velocity at the lowest gate at 15 m agl. The correlation coefficients for each regime seem to decay exponentially within the lowest 35 m of the boundary layer and linearly above 35 m. The correlations for the strong-wind regime decay more quickly with height than the correlations for the weak-wind regime. This implies that structures occurring under strong-wind conditions have smaller vertical extent than those occurring under weak-wind conditions. According to the correlation coefficients shown in Figure 5.7 the

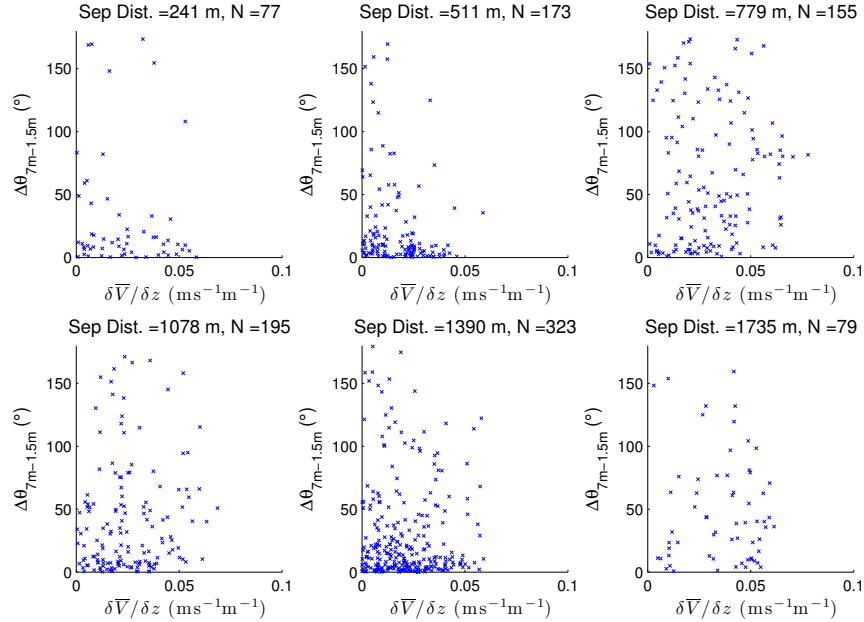


FIGURE 5.6: Wind direction difference between the upper and lower sonics plotted as a function of wind shear computed between 55 m agl and 115 m agl. Each data point represents a 16 minute average. These plots lack a clear signal thus indicating additional influences behind surface wind variability.

correlation between increasing height levels and the 15 meter height level decays more rapidly at short time scales. The rapid decay of short time-scaled structures implies that structures on short time scale occupy small vertical scales and that long time scales occupy larger spatial scales. The information shown in Figure 5.8 is based on the information seen in Figure 5.7. Each time the correlations in Figure 5.7 cross the threshold of e^{-1} the time-scale is plotted against the vertical separation distance resulting in Figure 5.8.

The relationship between vertical spatial and temporal scales appears to vary slightly between the weak and strong wind regimes.

5.2.2 Between-Station Correlations

In addition to the analysis of the vertical extent of surface layer processes, investigations were performed focusing on the horizontal behavior of structures as a function of height above ground (see Figures 5.9 and 5.10). As expected, we observe higher spectral

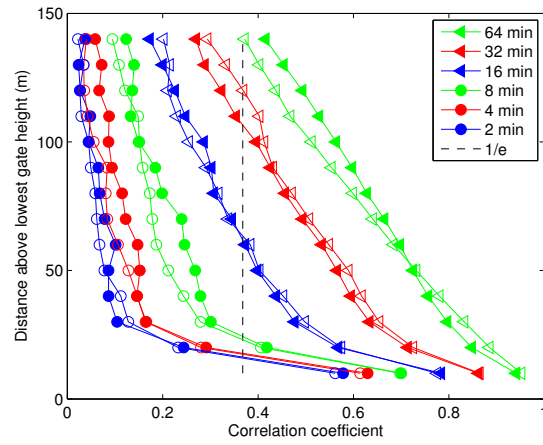
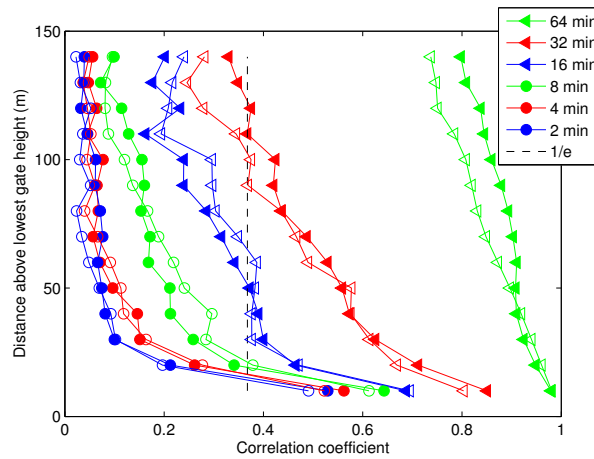
(a) $\bar{V}_{7m} \leq 1.5 m s^{-1}$ (b) $\bar{V}_{7m} > 1.5 m s^{-1}$

FIGURE 5.7: The correlation between increasing gate heights and the lowest possible gate height (15 m agl). Correlations are shown for all MRD time scales. The dotted line indicates the significance threshold of e^{-1} . Solid markers indicate correlations for the stationary SODAR and the open markers indicate correlations for the roving SODAR.

correlations at higher gates as the structures become larger with increasing height above ground.

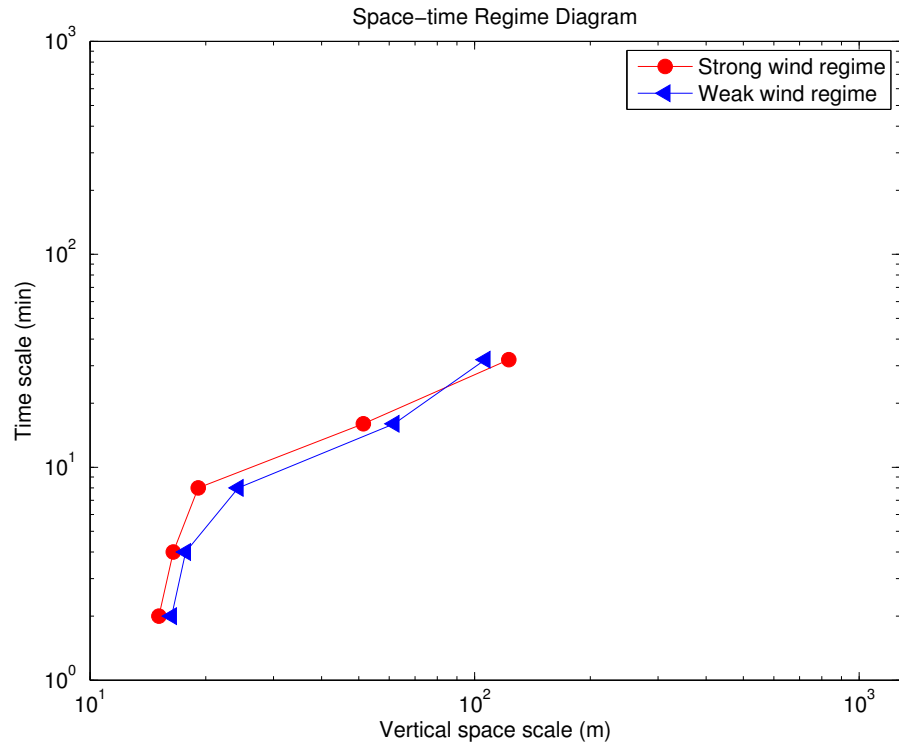


FIGURE 5.8: The relationship between vertical spatial and temporal scales for both weak wind and strong wind regimes. The point indicated with red circles represent the strong wind regime while the blue triangles indicate the weak wind regime. Each point represents the spatial separation between points and the time scale at which correlation coefficients cross the e^{-1} threshold indicated by the dotted line in Figure 5.7

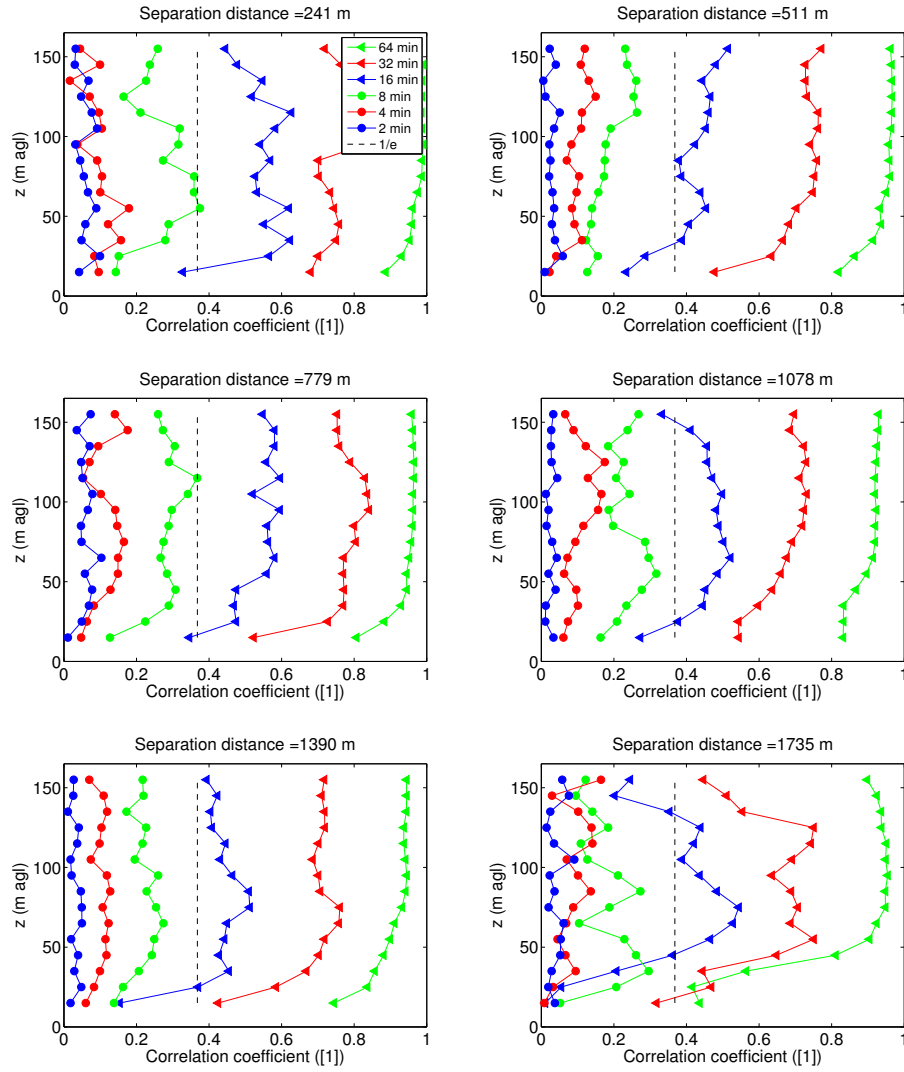


FIGURE 5.9: Correlations between stations as a function of height above ground for the weak wind regime. Each subplot represents a different SODAR separation distance. Coefficients are shown for each MRD time scale. The dotted line indicates a significance threshold of e^{-1} .

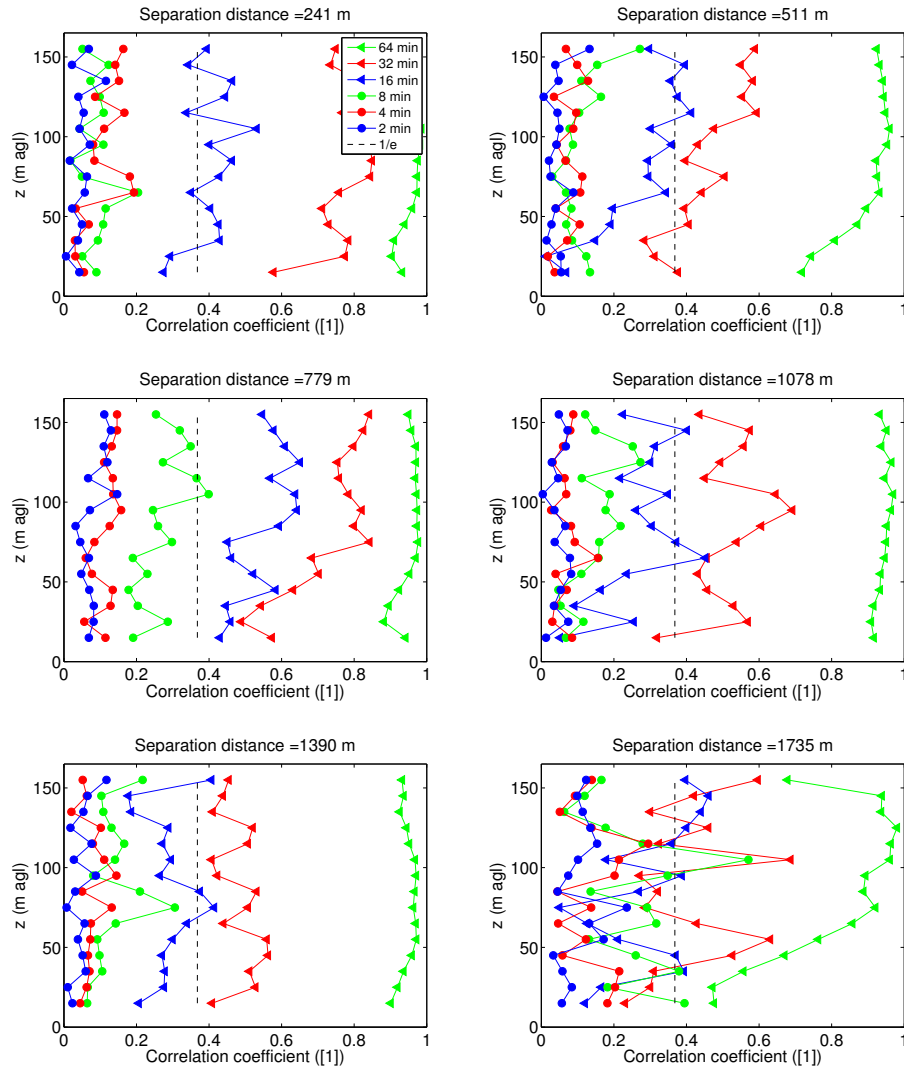


FIGURE 5.10: Correlation between stations as a function of height above ground for the strong wind regime. Coefficients are shown for each MRD time scale. The dotted line indicates the significance threshold of e^{-1} .

The correlation generally decreases with decreasing time scale, a result similar to that of the correlations between vertically separated gates (Section 5.2.1). Correlations are larger in the weak-wind regime (Figure 5.9) than they are in the strong-wind regime (Figure 5.10) indicating that structures under the strong-wind regime may occur on larger spatial scales than structures under the weak-wind regime. Correlations at time scales

of 2 minutes and 4 minutes fall below the e^{-1} significance threshold implying that at time scales below 8 minutes, structures are even smaller than the minimum SODAR separation distance. At time scales of 8 minutes, 16 minutes, 32 minutes and 64 minutes the correlations are weak near the surface but increase with increasing gate height. These correlations reach their maximum strength at approximately 55 m agl above which the correlations remain relatively constant with height. This indicates that the majority of the variability that could be influenced by sub-meso motions occurs within the lowest 55 meters of the SBL.

5.3. Horizontal Space-Time Analysis

The purpose of spacing the SODAR stations in increments was to acquire horizontal correlation statistics that could be used to construct a space-time regime diagram similar to Figure 2.3. Figure 5.11 shows the same increase in correlation with increasing time scale as seen in Figures 5.7, 5.9, and 5.10. The plots also show the correlation between stations decreasing with increasing separation distance. As in the previous analyses the correlations in the strong-wind regime appear to have a high level of variability compared to the weak-wind regime. The profiles Figure 5.3 exhibit high variability between each SODAR station separation distance. The variability between station configurations indicate unique weather patterns occurring during some of the separation intervals. This complicates the horizontal correlation analysis as the separation distance between the stations is not likely to be the only factor affecting differences in the SODAR measurements.

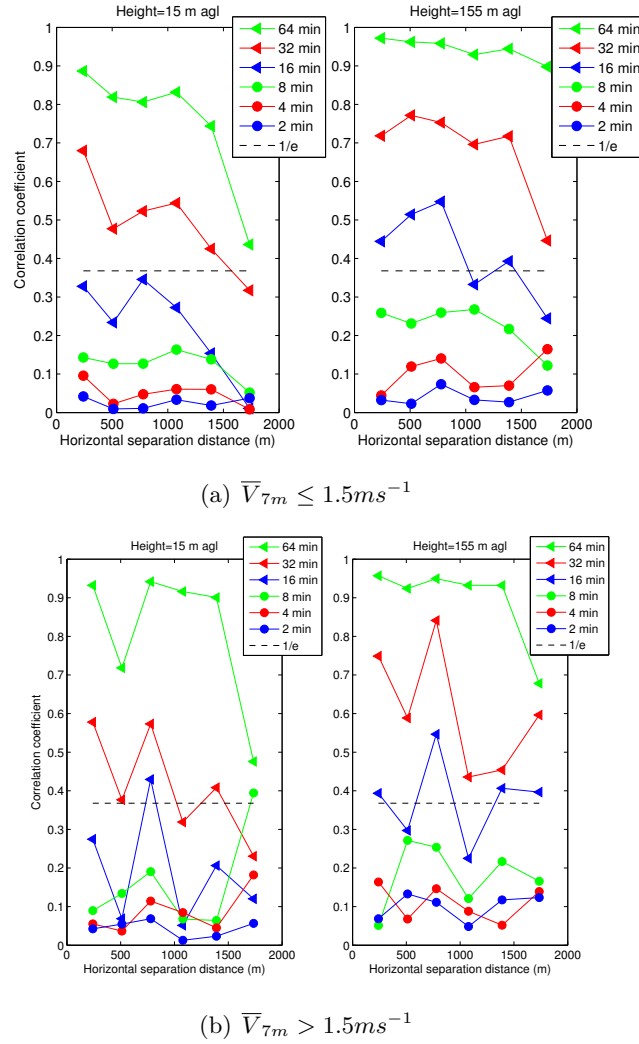


FIGURE 5.11: Figures show the correlation between each station configuration at 15 m agl (left) and 155 m agl (right). Correlations are shown as a function of MRD timescale. The dotted line represents the significance threshold of e^{-1}

5.4. Case studies

Bulk statistics, while useful when investigating long-term trends, are insufficient for diagnosing near-surface flow dynamics. In order to characterize weak-wind flow dynamics, short-term investigations were performed. Two nighttime periods were selected for case studies. The first case was chosen for its particularly weak winds and for its high directional

variability. The second case was selected because it exhibited both the development and the decay of a low level jet.

5.4.1 Case #1: High variability

The night of August 26th, 2010 was a period of generally weak winds with fluctuating wind speeds. These variations appear both aloft as well as near the surface. Figure 5.12 contains wind speed and direction profiles taken with the stationary SODAR for this case.

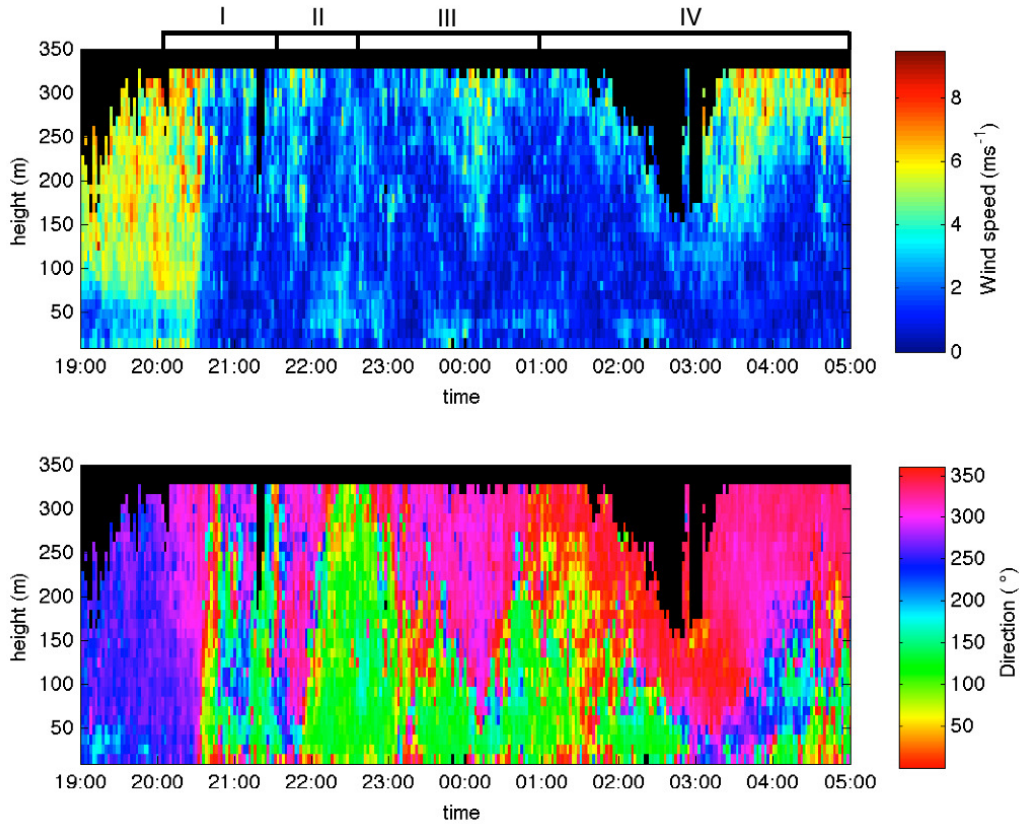


FIGURE 5.12: Wind speed and direction profiles taken using the stationary SODAR. Date: 08/26/2010 - 08/27/2010. Time: 20:00 - 05:00 PST.

The profiles in Figure 5.12 indicate 4 instances of interest for this study:

- I: (20:00 - 21:30) Transition from daytime to nighttime conditions.
- II: (21:30 - 22:30) Burst of northwesterly winds in the deeper boundary layer.

III: (22:30 - 01:00) Second burst of northwesterly winds in the deeper boundary layer.

IV: (01:00 - 05:00) Strong burst of northwesterly winds in the deeper boundary layer and transition from nighttime to daytime conditions.

Event I: Day-night transition

The transition from day into night is evident in Figure 5.12 as a period of high wind speeds ($\approx 4 - 6 \text{ ms}^{-1}$) followed by a sharp decrease in wind speeds. The wind is northwesterly before the transition but undergoes a large shift to the southeast.

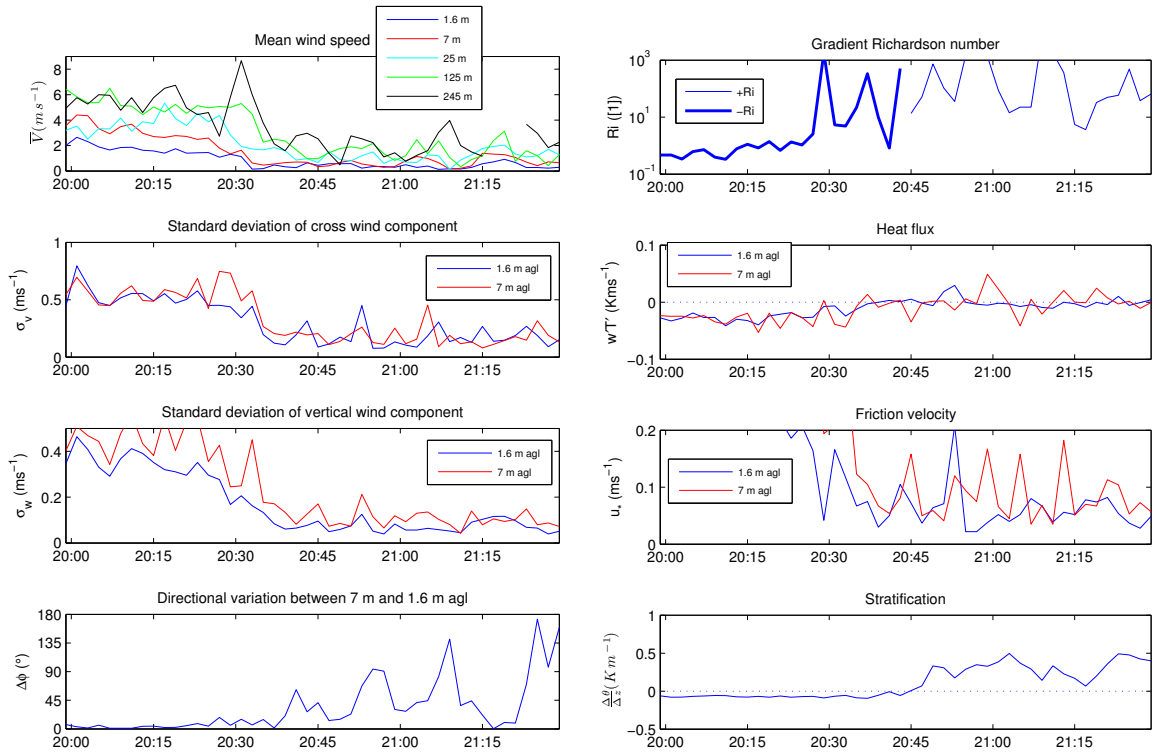


FIGURE 5.13: 2 minute time series of flow and stability data for 08/26 20:00 - 08/26 21:30. This period shows the transition between daytime and nighttime conditions.

Near-surface data taken using the sonic anemometers (see Figure 5.13) show that the transition from day to night is coupled with numerous effects on the flow and the stability.

After solar heating ceases, the stratification of the surface layer gradually becomes stable. At the same time the mean wind speed, cross wind component variability, and vertical wind variability decrease dramatically. The friction velocity decreases and the heat flux transitions from negative to positive along with the gradient Richardson number. As expected these changes are all coupled with a dramatic increase in directional variability between the upper and lower sonics. There is sequence of spikes in wind direction difference which, starting at approximately 20:35, occur every 15 minutes until the end of the period. These spikes correspond to sharp increases in cross wind variability.

Event II: First deep boundary layer burst

At approximately 21:30 there occurred an increase in mean wind speed in the deeper boundary layer that persisted until approximately 22:30. The increase in speed extended from the maximum SODAR range of 295 m agl to 125 m agl (see Figure 5.12). The strong event was coupled with a shift of the wind vector to northwesterly which can be seen from the maximum SODAR height to 55 m agl. The surface flow response is displayed in Figure 5.14. At approximately 21:50, wind speeds had increased at a height of 135 m agl. At approximately the same time, there occurred an increase in cross wind variability near the surface. The small vertical wind variability at that instance indicates a shift in horizontal motion without vertical mixing. At approximately 22:05 the wind speed in the deeper boundary layer decreased. The reduction of winds in the deep boundary layer is followed by an increase in wind speed in the lower 95 meters of the boundary layer. The strong increases in the cross wind variance and the vertical wind variance from 22:15 to 22:30 indicate strong turbulent mixing during this period.

Event III: Second deep boundary layer burst

The end of the previous strong wind speed event resulted in strong turbulent mixing and increased mean wind speed near the surface. Beginning at 23:30 wind speeds increased

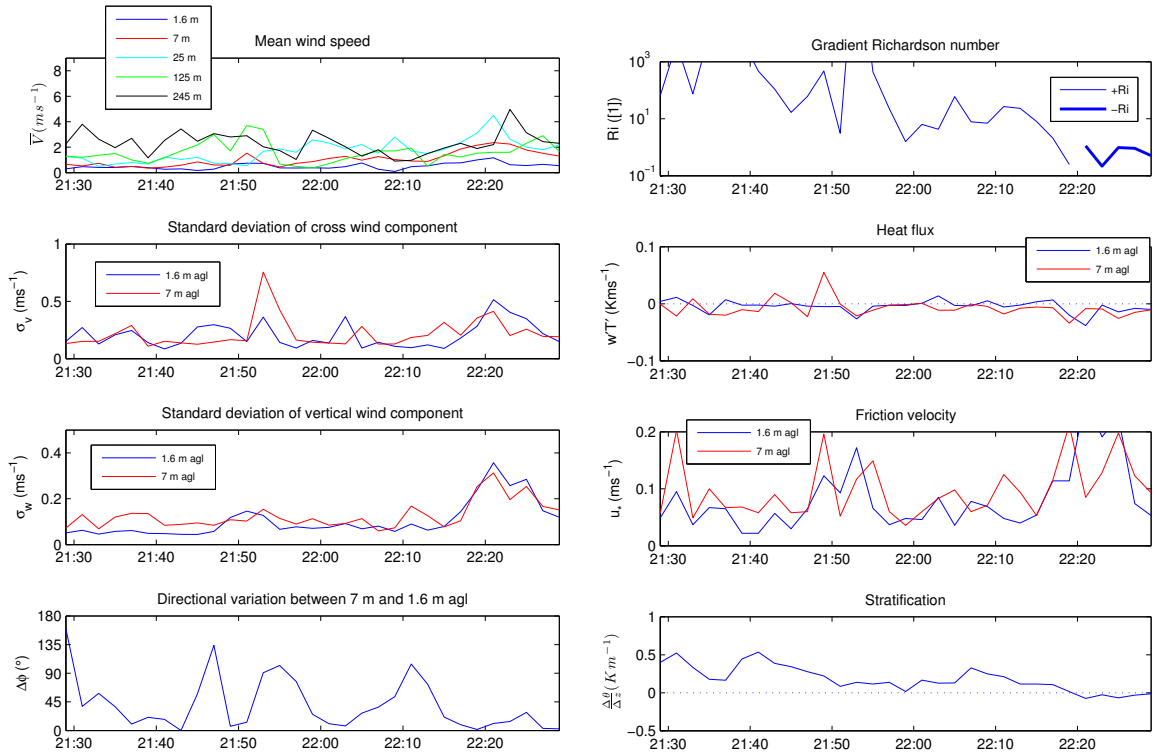


FIGURE 5.14: 2 minute time series of flow and stability data for 08/26 21:30 - 08/26 22:30. The effects of an acceleration event aloft on the surface flow is illustrated here.

above a height of 135 m agl. Similar to the previous event, this acceleration corresponds to a northwesterly shift in wind direction in the deeper boundary layer. Unlike the previous event however, the shift in wind direction only extends to 75 m agl. A brief but strong wind speed increase occurred at 25 m agl at 23:45. The surface effects depicted in Figure 5.15 show that for the majority of this case the surface layer is strongly stratified. At approximately 23:15 there occurred a brief burst of cross wind and vertical wind variance indicating a period of near-surface turbulence.

Event IV: Third burst and night-day transition

The fourth and final deeper boundary layer wind speed increase occurred during a period with a large amount of missing data present at the upper SODAR gates. As in the

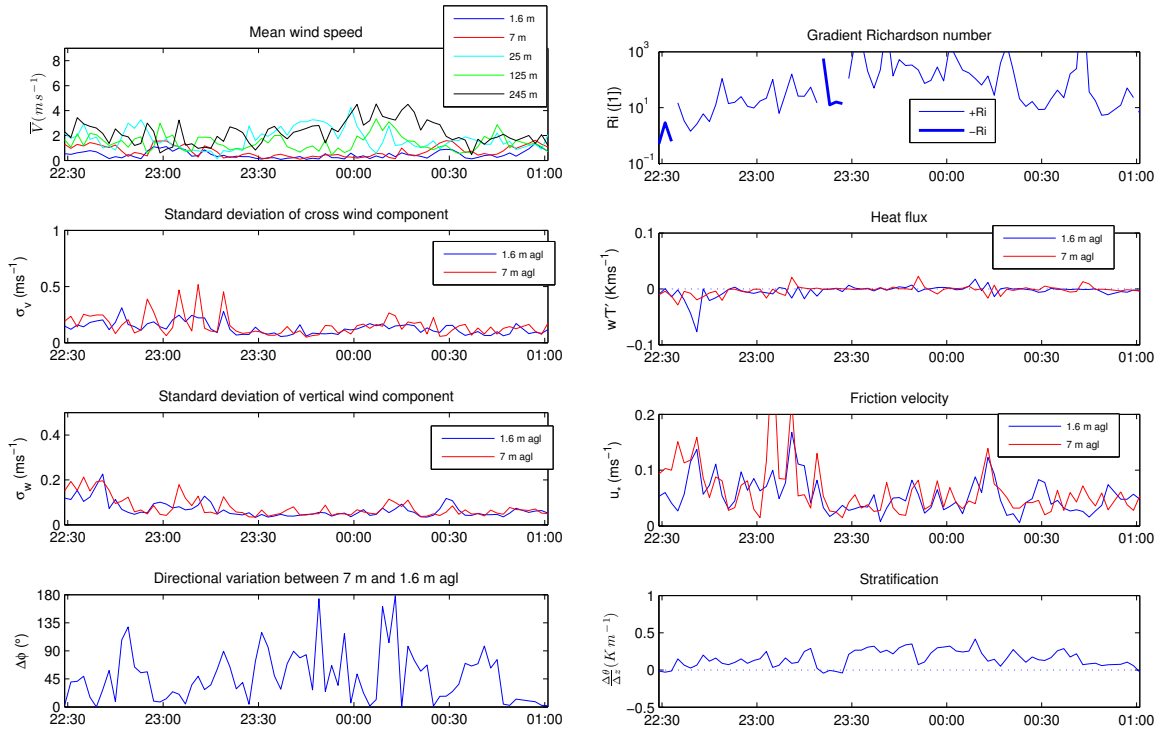


FIGURE 5.15: 2 minute time series of flow and stability data for 08/26 22:30 - 08/27 01:00. This event is similar to the previous event but persists for a longer period of time.

previous events, the upper level wind speed burst corresponds to a strong northwesterly wind. Between 15 m agl and 45 m agl there occurred a strong acceleration associated with a southeasterly wind. The wind profiles measured by the SODAR show strong vertical wind shear while the sonics show significant directional variability and weak mean winds. At approximately 04:30 the surface layer becomes unstably stratified and strong vertical mixing begins to occur (see Figure 5.16).

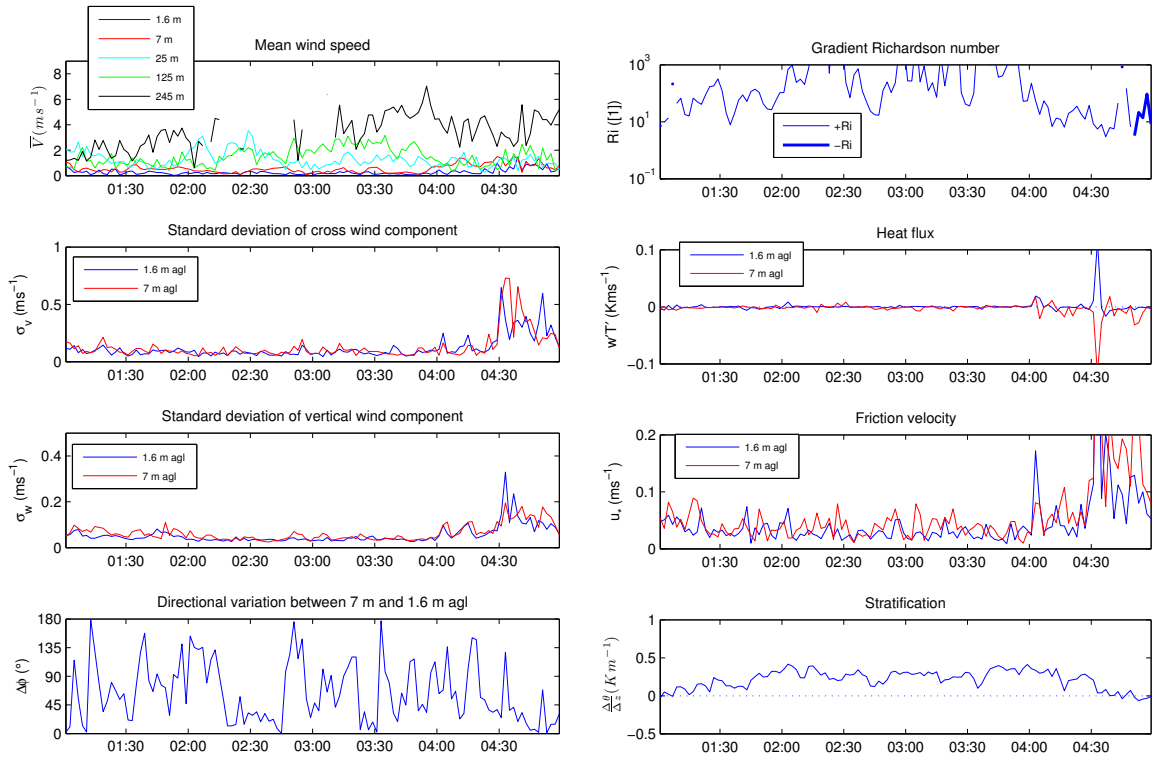


FIGURE 5.16: 2 minute time series of flow and stability data for 08/27 01:00 - 08/27 05:00. The surface flows occurring during this period are calm with limited variability until 04:00 when nighttime conditions begin to transition into daytime conditions.

5.4.2 Case #2: Low level jet

The night of October 2nd, 2010 began with the development of a low-level jet which persisted until 23:00 PST at which point it vanished. At 02:00 PST a second low-level jet began to form along with extreme directional variability near the surface. The wind speed and direction profiles measured by the stationary SODAR are shown in Figure 5.17.

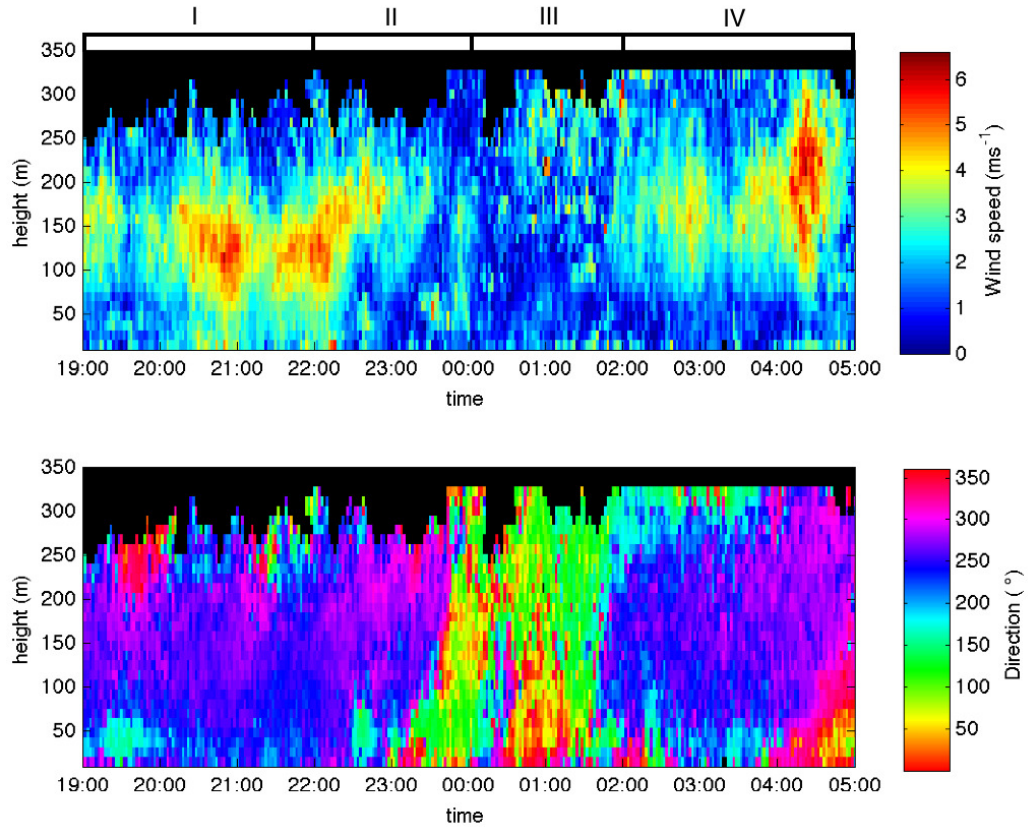


FIGURE 5.17: Wind speed and direction profiles taken using the stationary SODAR. Date: 10/02/2010 - 10/03/2010. Time: 19:00 - 05:00 PST.

Similar to the first case, the profiles in Figure 5.17 indicate 4 instances of interest for this study:

I: (19:00 - 22:00) Development of low-level jet.

II: (22:00 - 00:00) Decay of low-level jet.

III: (00:00 - 02:00) Weak wind period.

IV: (02:00 - 05:00) Development of second low-level jet.

Event I: Development of low-level jet

The low-level jet is characterized by positive vertical speed shear beneath the jet and strong negative vertical shear above. Possible causes of low-level jets include valley winds, sea breezes, inertial oscillations and fronts (Stull, 1988). In this case the low-level jet reaches a maximum wind speed at 21:00 and at an elevation of approximately 125 m agl. The direction of the low-level jet is northwesterly. Figure 5.18 shows significant

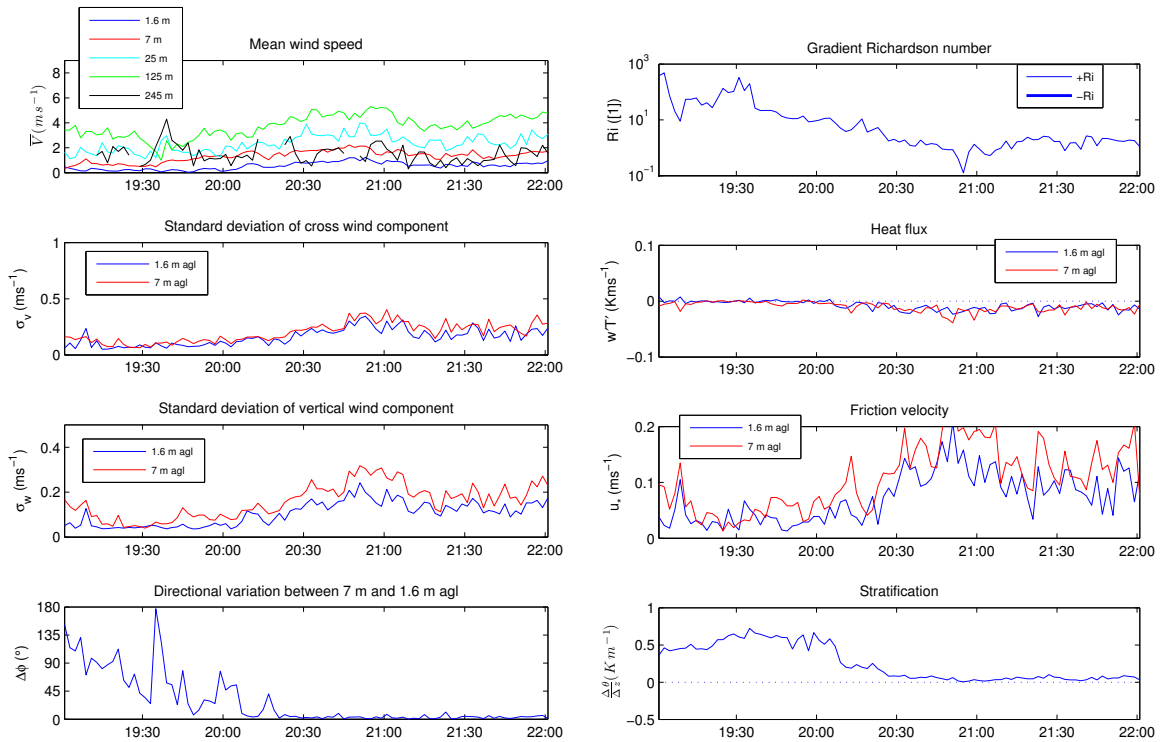


FIGURE 5.18: 2 minute time series of flow and stability data for 10/02 19:00 - 22:00. Data shown here occurs beneath a low-level jet.

directional variability during the period of time preceding the development of the low-level jet. Once the low level jet is established, the directional variability between the sonics

decreases and the surface layer transitions from stable to neutral stratification. The period of weakened stratification coincides with a period of strong turbulence. The vertical size of the turbulent eddies must be equal to or greater than the distance between the two sonics in order for the sonic direction measurements to be equal.

Event II: Decay of low-level jet

This second event of interest in this case is the decay of the low-level jet leading into a period of high directional fluctuations and reduced mean wind speeds. At 22:00 the maximum of the low-level jet appears to move upward as the winds gradually decay. The jet halts its ascent at approximately 195 m agl before decreasing below 2 ms^{-1} near midnight. As the low-level jet decays, the surface-layer stratification grows more stable and

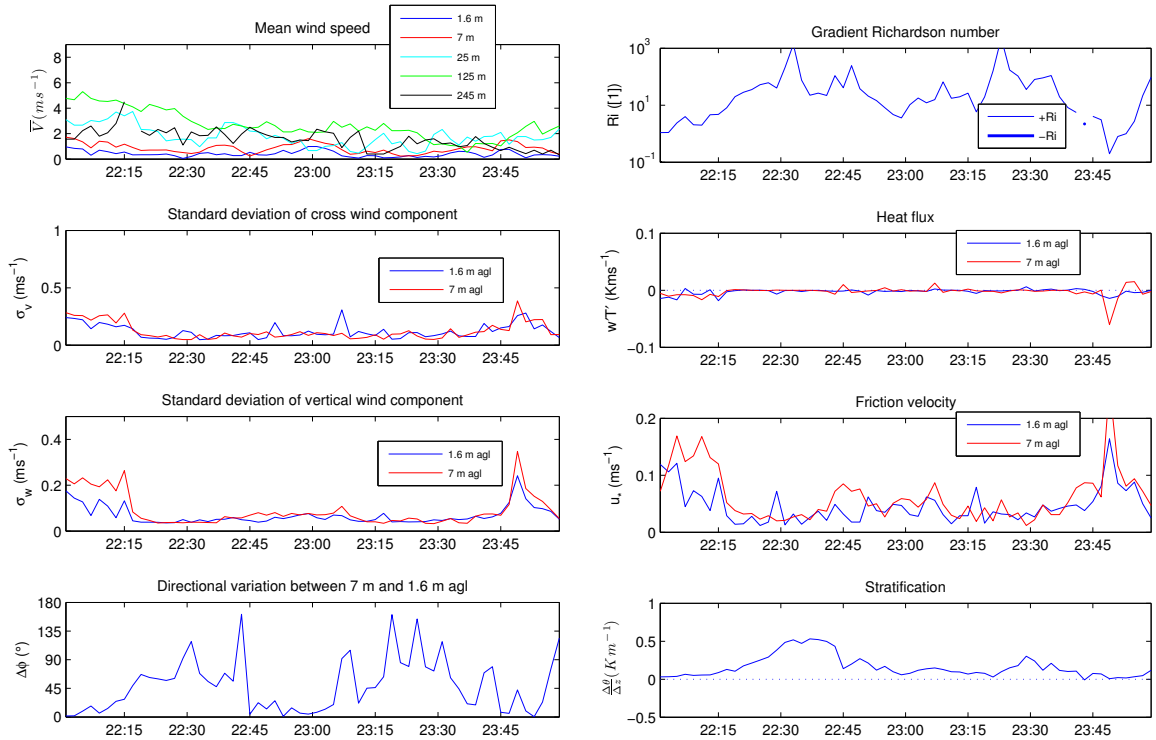


FIGURE 5.19: 2 minute time series of flow and stability data for 10/02 22:00 - 10/03 00:00. This period follows the surface flows occurring during the decay of a low-level jet.

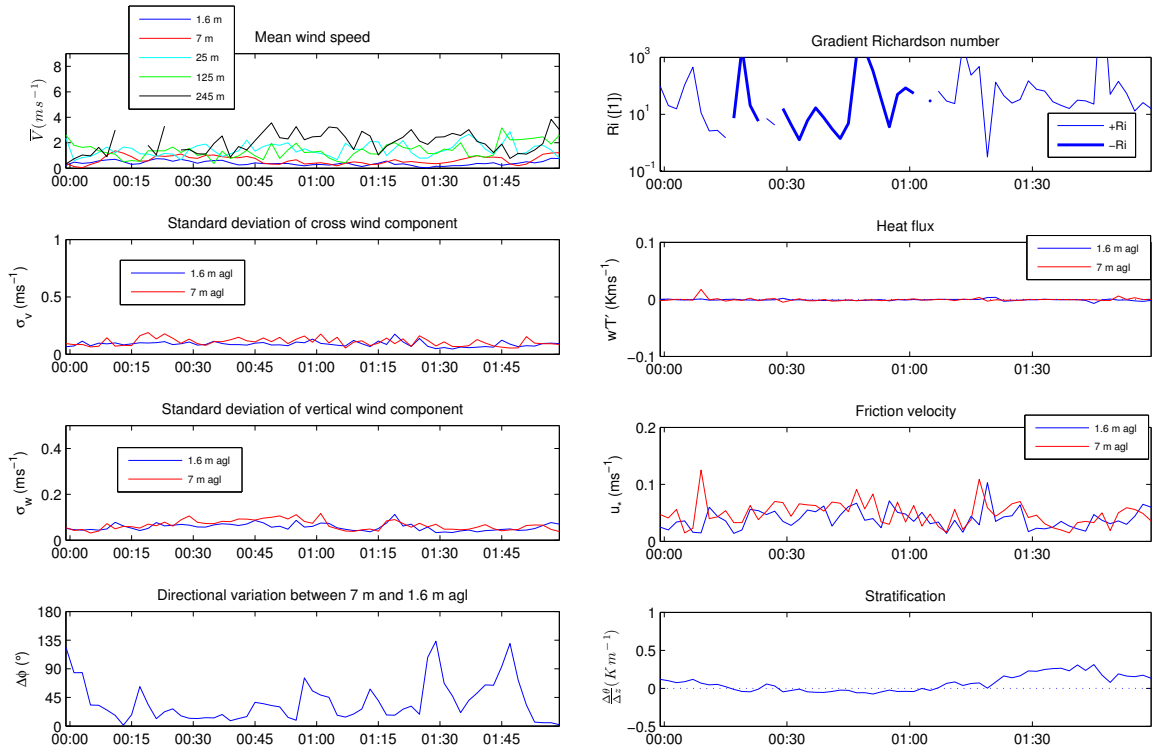


FIGURE 5.20: 2 minute time series of flow and stability data for 10/03 00:00 - 10/03 02:00.

the strength of turbulence is reduced (see Figure 5.19). In addition to reduced turbulence, directional variability between the sonics is increased. This effect indicates that stable stratification increases near-surface flow variability.

Event III: Weak-wind period

The third event takes place during a period of generally weak winds with high directional variability at all SODAR gates. The flow appears to meander between northerly and southeasterly flows. The third period shows moderate directional variability between the sonics. The temperature profile transitions between weakly stable and weakly unstable stratification (See Figure 5.20). According to the net radiation time series seen in Figure 5.21 the third event is preceded by a period of increased net radiation. This increase in

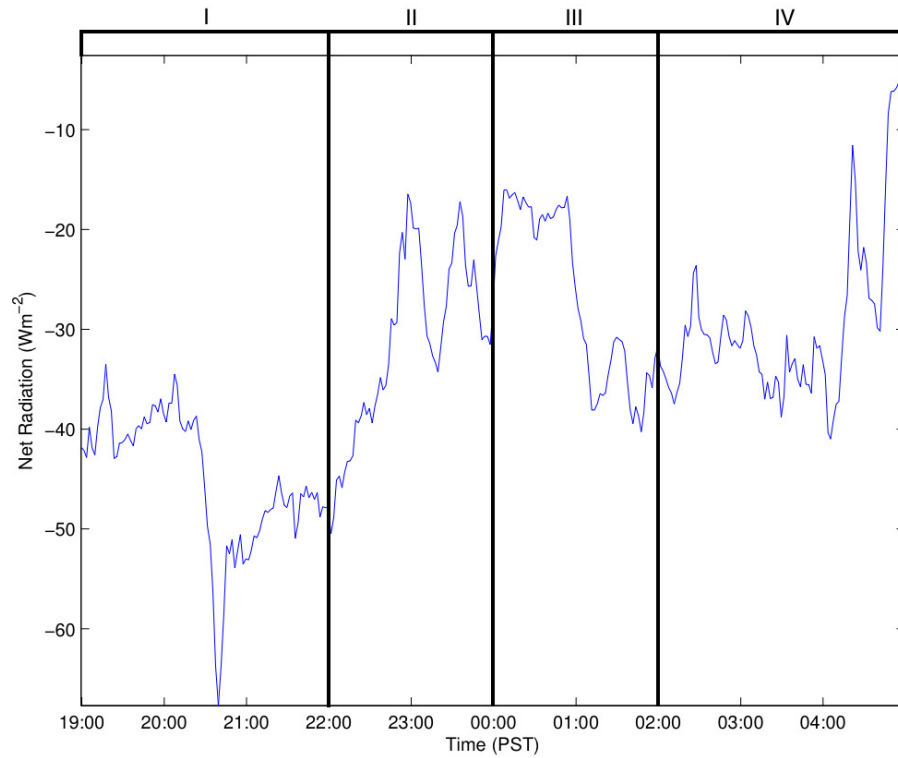


FIGURE 5.21: The net radiation corresponding to the night of case 2. Fluctuations in net radiation between 23:00 and 01:00 indicate the presence of sporadic cloud cover.

net radiation could indicate partial cloud coverage which could act to slow the radiative cooling of the surface and weaken the stratification near the surface.

Event IV: Second low-level jet and transition from night to day

The final event for this case exhibits the development of a second low-level jet centered at approximately 155 m agl. This jet is weaker than the first and occurs at a higher elevation. This period exhibits weak turbulence and the stability near the surface is quite strong. The stability decreases gradually beginning at 03:30 and continuing through the end of the period. As in the previous cases, the wind direction variability is significantly increased under strong stable stratification.

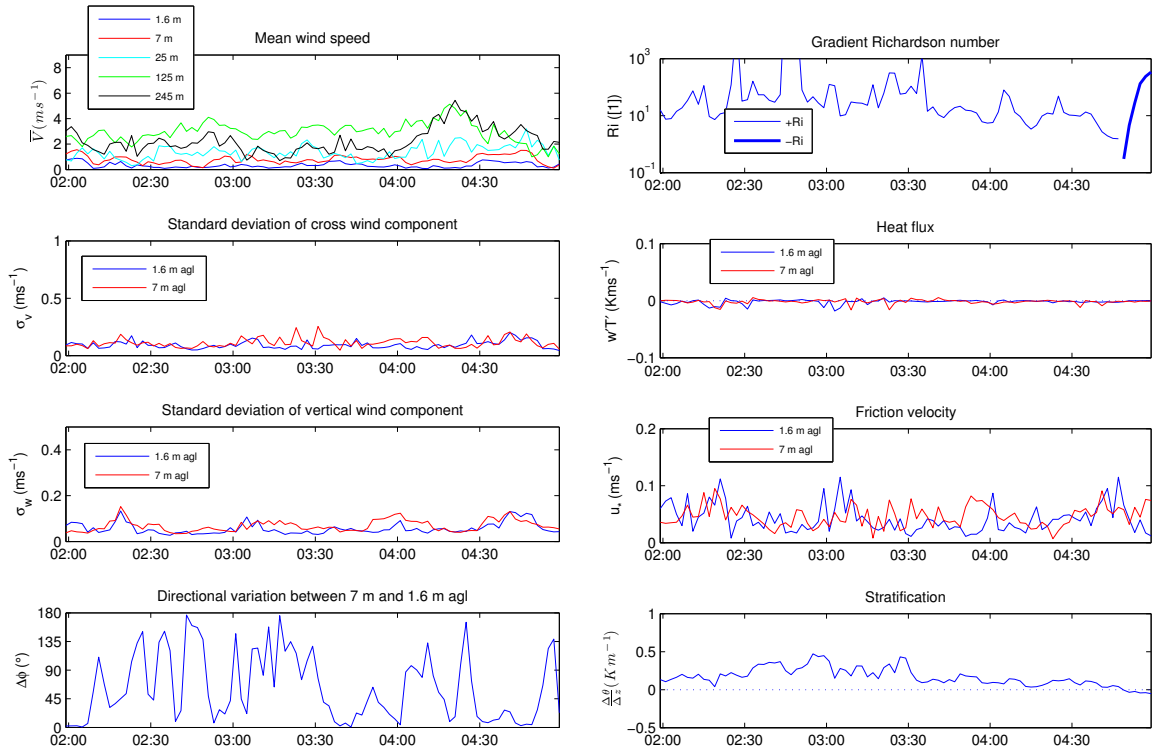


FIGURE 5.22: 2 minute resolution time series of flow and stability data for 10/03 02:00 - 10/03 04:50. During this period a new low level jet develops at a height of 155 m agl.

6. CONCLUSIONS

The overarching goal of this research was to improve the understanding of the influence of forcing from the deeper boundary layer over weak wind surface layer variability. Data was taken during the DONUTSS-2010 field campaign using a pair of SODAR stations. Data quality has been assured by the internal error checking routines of the Metek PCS.2000/MF-24 SODAR system as well as through comparison of the two SODARs measurements. The following conclusions can be made based on the results of this study:

- The SODAR system is adequate when obtaining data on sub-meso scales and the necessary spatial coverage that was lacking in previous work can be achieved with this instrument. However, if horizontal correlation analyses are to be performed with separation distance the use of multiple SODAR systems simultaneously is advised.
- SODAR systems are very sensitive to noise when set to a short averaging interval. The use of a setting above 2 minutes is recommended in future experiments. Also, much of the day time data taken during this experiment was filtered out due to noise constraints imposed by the nearby highway. Thus great care must be taken when placing a SODAR system in order to avoid contamination due to broadband noise.
- At short averaging intervals, the cluster averaging method provides higher quality data than the more commonly used spectral averaging method. The cluster method is less sensitive to the influence of outliers in the backscattered spectra.
- Correlation coefficients computed between SODAR stations decrease at heights below 55 m agl. This decrease indicates that the majority of the wind variability occurring in the SBL occurs within the lowest 55 meters of the SBL.
- In general, all correlation statistics show an increase in spatial extent with time scale. This means that for boundary layer structures within the SBL, spatial and

temporal scales are related but the extent of that relationship remains unclear. We therefore cannot prove or disprove Taylor's hypothesis.

- Significant near-surface wind direction variability occurs most frequently during periods when the wind speed measured at 7 m agl is less than 1.5 ms^{-1} .
- Case studies have not provided evidence suggesting a connection between near-surface flow and deeper boundary layer forcing under strong stratification. The night of August 26th, 2010 has demonstrated that under strongly stable conditions, near-surface flow dynamics are decoupled from deeper boundary layer forcing.
- The low-level jets which occurred during the night of October 2nd, 2010 were able to influence flow near the surface but only when they occurred sufficiently close to the surface. This is demonstrated first by the first low-level jet, which occurred from 20:30 to 23:00 centered at a height of approximately 135 m agl. The second low-level jet occurred that same night from 02:00 to 05:00 centered at approximately 185 m agl and did not influence near-surface stratification and flow dynamics.

The sequential separation of the SODAR systems resulted in 6 independent data sets to be used in correlation analysis. The independence of these data sets resulted in complications when attempting to draw conclusions from the behavior of correlations between stations with separation distance. In order to more adequately measure the horizontal extents of motions within the deeper boundary layer, the use of more than two SODAR systems is recommended. Another possible solution to this problem would be to more carefully select individual periods from the 6 separate data sets according to synoptic conditions.

BIBLIOGRAPHY

- Anfossi, D., D. Oetzel, G. Degrazia, and A. Goulart, 2005: An analysis of sonic anemometer observations in low wind speed conditions. *Boundary-Layer Meteorology*, **114**, 179–203.
- Argentini, S., G. Mastrantonio, I. Petenko, I. Pietroni, and A. Viola, 2012: Use of high-resolution sodar to study surface-layer turbulence at night. *Boundary-Layer Meteorology*, **143**, 177–188.
- Arya, S., 2001: *Introduction to Micrometeorology*. Intern. Geophys. Ser., Academic Press, San Diego, CA.
- Beylkin, G., R. Coifman, and V. Rokhlin, 1991: Fast wavelet transforms and numerical algorithms 1. *Communications on Pure and Applied Mathematics*, **44** (2), 141–183.
- Blokhintzev, D., 1946: The propagation of sound in an inhomogeneous and moving medium i and ii. *J. Acoust. Soc. Amer.*, **18**, 322–334.
- Coulter, R. and M. Kallistratova, 2004: Two decades of progress in sodar techniques: A review of 11 isars proceedings. *Meteorology and Atmospheric Physics*, **85**, 3–19.
- Crescenti, G. H., 1998: The degradation of doppler sodar performance due to noise: A review. *Atmos. Environ.*, **32**, 1499–1509.
- Giancoli, D., 2000: *Physics for Scientists and Engineers*. Prentice Hall, Upper Saddle River, NJ.
- Harris, C. M., 1966: Absorption of sound in air versus humidity and temperature. *J. Acoust. Soc. Amer.*, **40**, 149–159.
- Howell, J. and L. Mahrt, 1994: An adaptive multiresolution data filter: applications to turbulence and climatic time series. *Amer. Meteorol. Soc.*, **51**, 2165–2177.

- Howell, J. F. and L. Mahrt, 1997: Multiresolution flux decomposition. *Boundary-Layer Meteorology*, **83** (1), 117–137.
- Kaimal, J. and J. Finnigan, 1994: *Atmospheric Boundary Layer Flows: Their Structure and Measurements*. Oxford University Press, New York, NY.
- Kallistratova, M., 1997: Physical grounds for acoustic remote sensing of the atmospheric boundary layer. *Acoustic Remote Sensing Applications*, S. Singal, Ed., Narosa Publishing House, New Delhi, India, 3–34.
- Katul, G. and M. Parlange, 1995: Analysis of land surface heat fluxes using the orthonormal wavelet approach. *Water Resources Research*, **31** (11), 2743–2749.
- Kraichnan, R. H., 1953: The scattering of sound in a turbulent medium. *J. Acoust. Soc. Amer.*, **25**, 1096–1104.
- Lines, I., D. Deaves, and W. Atkins, 1997: Practical modelling of gas dispersion in low wind speed conditions. *J. Hazard. Mater.*, **54**, 201–226.
- Little, C. G., 1969: Acoustic methods for the remote probing of the lower atmosphere. *Proc. IEEE*, **57**, 571–578.
- Mahrt, L., 2007: The influence of nonstationarity on the turbulent flux-gradient relationship for stable stratification. *Boundary-Layer Meteorology*, **125**, 245–264.
- Mahrt, L., 2008a: The influence of transient flow distortion on turbulence in stable weak-wind conditions. *Boundary-Layer Meteorology*, **127**, 1–16.
- Mahrt, L., 2008b: Mesoscale wind direction shifts in the stable boundary-layer. *Tellus Series A-Dynamic Meteorology and Oceanography*, **60A**, 700–705.
- Mahrt, L., 2010: Computing turbulent fluxes near the surface: Needed improvements. *Ag. For. Meteorol.*, **150**, 501–509.

- Mahrt, L. and J. Howell, 1994: The influence of coherent structures and microfronts on scaling laws using global and local transforms. *J. Fluid Mech.*, **260**, 247–270.
- Mahrt, L. and R. Mills, 2009: Horizontal diffusion by submeso motions in the stable boundary layer. *Environ. Fluid Mech.*, **9**, 443–456.
- Mahrt, L., C. Thomas, and J. Prueger, 2009: Space-time structure of mesoscale motions in the stable boundary layer. *Q. J. R. Meteorol. Soc.*, **135**, 67–75.
- Meyer, J. C., 2005: Characterisation of the atmospheric boundary layer in a complex terrain using sodar-rass. Ph.D. thesis, University of Bayreuth.
- Moulsley, T. J., R. S. Cole, D. N. Asimakopoulous, and S. J. Caughey, 1979: Simultaneous horizontal and vertical acoustic sounding of the atmospheric boundary layer. *Boundary-Layer Meteorology*, **19**, 359–372.
- Neff, W. D., 1975: Quantitative evaluation of acoustic echoes from the planetary boundary layer. Tech. rep., NOAA.
- Neff, W. D., 1978: Beamwidth effects on acoustic backscatter in the planetary boundary layer. *J. Appl. Meteorol.*, **17**, 1514–1520.
- Shore, J. E., 1973: On the application of haar functions. *IEEE Trans. Commun.*, **21**, 209–216.
- Stull, R., 1988: *An introduction to boundary layer meteorology*. Kluwer Academic Publisher, Dordrecht.
- Sun, J., et al., 2004: Atmospheric disturbances that generate intermittent turbulence in nocturnal boundary layers. *Boundary-Layer Meteorology*, **110** (2), 255–279.
- Taylor, G., 1938: The spectrum of turbulence. *Proc. Roy. Soc. London*, **A164**, 476–490.

- Thomas, C., 2011: Variability of sub-canopy flow, temperature, and horizontal advection in moderately complex terrain. *Boundary-Layer Meteorology*, **139**, 61–81.
- Thomas, C., A. M. Kennedy, J. S. Selker, A. Moretti, M. H. Schroth, A. R. Smoot, N. B. Tuffillaro, and M. J. Zeeman, 2012: High-resolution fibre-optic temperature sensing: A new tool to study the two-dimensional structure of atmospheric surface layer flow. *Boundary-Layer Meteorology*, **142**, 177–192.
- Tyndall, J., 1874: On the atmosphere as a vehicle for sound. *Phil. Trans. Roy. Soc.*, **164**, 183 – 244.
- Wyngaard, J. C., Y. Izumi, and S. A. Collins Jr., 1971: Behavior of the refraction-index-structure parameter near the ground. *J. Acoust. Soc. Amer.*, **61**, 1646–1650.

APPENDICES

A APPENDIX A SODAR Spectral Analysis

From: Metek PCS.2000/MF-24 User Manual, Chapter: Signal Analysis Doppler-SODAR pgs. 5-8.

First, before every pulse the SODAR makes two independent noise measurements in which the Fast-Fourier transform is used to compute 32 complex numbers for the amplitude of the background noise.

$$R1_n(n = 1...32) \quad (A.1)$$

$$R2_n(n = 1...32) \quad (A.2)$$

Then, for each pulse and each height, the Fast-Fourier transform is used to compute 32 complex numbers for the amplitude of the signal.

$$E_n(n = 1...32) \quad (A.3)$$

The residual power is given when the averaged noise is subtracted from the received signal:

$$S_n = \left(E_n - \frac{R1_n + R2_n}{2} \right) (n = 1...32) \quad (A.4)$$

The derived power spectrum is approximated by a Gaussian shaped model function:

$$P = \frac{pwr \Delta f}{sig \sqrt{2\pi}} e^{-\frac{1}{2} \left(\frac{freq-f}{sig} \right)^2} \quad (A.5)$$

$$\Delta f = \frac{c}{2\Delta h} \quad (A.6)$$

Where Δh is the height range, c is the speed of sound, and f is the frequency

estimate. Sound speed is computed with a temperature measurement made by a PT-100 probe according to:

$$c = 20.05\sqrt{T} \quad (\text{A.7})$$

The sequential numbering in the FFT lines can be seen as a frequency shift according to:

$$f_n = (n - 16)\Delta f \quad (\text{A.8})$$

For the approximation of power spectra, only the line within a certain area neighboring the main spectral peak are considered. This reduces the sensitivity to broad band noise contribution. This area is determined by a threshold of 25% of the maximum peak which corresponds to a 6 dB decrease from the maximum signal intensity. So a number of spectral lines n is defined within such 6 dB area which are used to compute the regression between the model and the measured power spectra. The values of pwr , frq , and sig are called moments of the density function.

pwr represents the area under the gaussian shaped curve and is the total power of the signal. frq is the center of gravity on the frequency axis and is the most likely value for the frequency shift of the signal. sig is the standard deviation of the distributed intensities, it corresponds to the width of the spectrum.

For mathematical reasons logarithmic values of the power spectra are used for further evaluation. Doing so transforms the Gaussian shaped distribution into a parabolic which is easier to handle. The parameters are derived from the spectrum as follows:

$$frq = -0.5 \frac{D_1}{D_2} \quad (\text{A.9})$$

$$sig = -0.5 \frac{D}{D_2} \quad (\text{A.10})$$

$$pwr = sig\sqrt{2\pi}e^{\left(\frac{D_2}{D}frq^2 + \frac{D_1}{D}frq + \frac{D_0}{D}\right)} \quad (A.11)$$

These are computed according to:

$$\begin{aligned} f(a, b, c) &= \sum_{i=1}^n (y_i - ax_i^2 - bx_i - c)^2 \\ &= \sum_{i=1}^n y_i^2 - 2 \sum_{i=1}^n y_i ax_i^2 - 2 \sum_{i=1}^n y_i bx_i^2 - 2 \sum_{i=1}^n cy_i + 2 \sum_{i=1}^n abx_i^3 \\ &\quad + 2 \sum_{i=1}^n acx_i^2 + \sum_{i=1}^n b^2 x_i^2 + 2 \sum_{i=1}^n bcx_i^2 + \sum_{i=1}^n a^2 x_i^4 + \sum_{i=1}^n c^2 \end{aligned} \quad (A.12)$$

If $f(a, b, c) \rightarrow \min$

$$\begin{aligned} \frac{\partial f}{\partial a} &= -2 \sum_{i=1}^n y_i x_i^2 + 2 \sum_{i=1}^n bx_i^3 + 2 \sum_{i=1}^n cx_i^2 + 2 \sum_{i=1}^n ax_i^4 = 0 \\ \Rightarrow a \sum_{i=1}^n x_i^4 + b \sum_{i=1}^n x_i^3 + c \sum_{i=1}^n x_i^2 &= \sum_{i=1}^n y_i x_i^2 \end{aligned} \quad (A.13)$$

$$\begin{aligned} \frac{\partial f}{\partial b} &= -2 \sum_{i=1}^n y_i x_i + 2 \sum_{i=1}^n ax_i^3 + 2 \sum_{i=1}^n bx_i^2 + 2 \sum_{i=1}^n cx_i = 0 \\ \Rightarrow a \sum_{i=1}^n x_i^3 + b \sum_{i=1}^n x_i^2 + c \sum_{i=1}^n x_i &= \sum_{i=1}^n y_i x_i \end{aligned} \quad (A.14)$$

$$\begin{aligned} \frac{\partial f}{\partial c} &= -2 \sum_{i=1}^n y_i + 2 \sum_{i=1}^n ax_i^2 + 2 \sum_{i=1}^n bx_i + 2 \sum_{i=1}^n c = 0 \\ \Rightarrow a \sum_{i=1}^n x_i + b \sum_{i=1}^n x_i + cn &= \sum_{i=1}^n y_i x_i \end{aligned} \quad (A.15)$$

$$D = \begin{vmatrix} \sum_{i=1}^n x_i^4 & \sum_{i=1}^n x_i^3 & \sum_{i=1}^n x_i^2 \\ \sum_{i=1}^n x_i^3 & \sum_{i=1}^n x_i^2 & \sum_{i=1}^n x_i \\ \sum_{i=1}^n x_i^2 & \sum_{i=1}^n x_i & n \end{vmatrix} \quad D_0 = \begin{vmatrix} \sum_{i=1}^n x_i^4 & \sum_{i=1}^n x_i^3 & \sum_{i=1}^n y_i x_i^2 \\ \sum_{i=1}^n x_i^3 & \sum_{i=1}^n x_i^2 & \sum_{i=1}^n y_i x_i \\ \sum_{i=1}^n x_i^2 & \sum_{i=1}^n x_i & n \end{vmatrix}$$

$$D_1 = \begin{vmatrix} \sum_{i=1}^n x_i^4 & \sum_{i=1}^n y_i x_i^2 & \sum_{i=1}^n x_i^2 \\ \sum_{i=1}^n x_i^3 & \sum_{i=1}^n y_i x_i & \sum_{i=1}^n x_i \\ \sum_{i=1}^n x_i^2 & \sum_{i=1}^n y_i & n \end{vmatrix} \quad D_2 = \begin{vmatrix} \sum_{i=1}^n y_i x_i^2 & \sum_{i=1}^n x_i^3 & \sum_{i=1}^n x_i^2 \\ \sum_{i=1}^n y_i x_i & \sum_{i=1}^n x_i^2 & \sum_{i=1}^n x_i \\ \sum_{i=1}^n y_i & \sum_{i=1}^n x_i & n \end{vmatrix}$$

$$\begin{aligned} D &= n \sum_{i=1}^n x_i^2 \sum_{i=1}^n x_i^4 + 2 \sum_{i=1}^n x_i \sum_{i=1}^n x_i^2 \sum_{i=1}^n x_i^3 \\ &\quad - \left(\sum_{i=1}^n x_i^2 \right)^3 - \left(\sum_{i=1}^n x_i \right)^2 \sum_{i=1}^n x_i^4 - n \left(\sum_{i=1}^n x_i^3 \right)^2 \end{aligned} \quad (\text{A.16})$$

$$\begin{aligned} D_0 &= \sum_{i=1}^n y_i \sum_{i=1}^n x_i^2 \sum_{i=1}^n x_i^4 + \sum_{i=1}^n x_i \sum_{i=1}^n x_i^2 y_i \sum_{i=1}^n x_i^3 + \sum_{i=1}^n x_i y_i \sum_{i=1}^n x_i^2 \sum_{i=1}^n x_i^3 \\ &\quad - \left(\sum_{i=1}^n x_i^2 \right)^2 \sum_{i=1}^n x_i^2 y_i - \sum_{i=1}^n x_i \sum_{i=1}^n x_i y_i \sum_{i=1}^n x_i^4 - \sum_{i=1}^n y_i \left(\sum_{i=1}^n x_i^3 \right)^2 \end{aligned} \quad (\text{A.17})$$

$$\begin{aligned} D_1 &= n \sum_{i=1}^n x_i y_i \sum_{i=1}^n x_i^4 + \sum_{i=1}^n y_i \sum_{i=1}^n x_i^2 \sum_{i=1}^n x_i^3 + \sum_{i=1}^n x_i \sum_{i=1}^n x_i^2 \sum_{i=1}^n x_i^2 y_i \\ &\quad - \sum_{i=1}^n x_i y_i \left(\sum_{i=1}^n x_i^2 \right)^2 - \sum_{i=1}^n y_i \sum_{i=1}^n x_i \sum_{i=1}^n x_i^4 - n \sum_{i=1}^n x_i^2 y_i \sum_{i=1}^n x_i^3 \end{aligned} \quad (\text{A.18})$$

$$\begin{aligned} D_2 &= n \sum_{i=1}^n x_i^2 \sum_{i=1}^n x_i^2 y_i + \sum_{i=1}^n x_i \sum_{i=1}^n x_i y_i \sum_{i=1}^n x_i^2 + \sum_{i=1}^n y_i \sum_{i=1}^n x_i \sum_{i=1}^n x_i^3 \\ &\quad - \sum_{i=1}^n y_i \left(\sum_{i=1}^n x_i^2 \right)^2 - \left(\sum_{i=1}^n x_i \right)^2 \sum_{i=1}^n x_i^2 y_i - n \sum_{i=1}^n x_i y_i \sum_{i=1}^n x_i^3 \end{aligned} \quad (\text{A.19})$$

B APPENDIX B SODAR Error Codes

The following table shows a breakdown of the possible error codes and their meaning in terms of spectral analysis. Each code is unique such that any digit is either represented as a single error code or the sum of two or three error codes (e.g error code 00007 means that 00001, 00002, and 00004 all apply). During the data quality control phase, only data that passed all of the critical error codes were used. Critical error codes include the following:

- 00004
- 00020
- 00040
- 00400
- 01000
- 02000

TABLE 0.1: Key illustrating the possible error codes reported by the SODAR software. The codes are written such that all combinations of digits are unique.

Bit	Octal Code	Meaning
0	00001	Saturation of the receiver for one or several samples. The affected instantaneous spectra are rejected and not used in the averaging process. The measurements are not influenced by the saturation events.
1	00002	High level of white noise for one or several samples. The affected instantaneous spectra are rejected and not used in the averaging process. The measurements are not influenced by the white noise events.
2	00004	Local maximum in the spectra too strong as compared to the main/absolute maximum. Local maxima can be generated by fixed echoes, high ambient noise of certain frequencies. The computed radial components and all derived values are invalid.
4	00020	Signal/Noise ratio too low. The computed radial components and all derived values are invalid.
5	00040	Low statistical significance of the measured backscattered acoustic signal. Most of the instantaneous signal spectra have been rejected. The computed radial components and all derived values are invalid.
6	00100	Low statistical significance of the measured ambient noise. Most of the instantaneous noise spectra have been rejected.
8	00400	The maximum of the averaged signal spectrum is too slim as compared to the theoretical value. The computed radial components and all derived values are invalid.
9	01000	The maximum of the averaged signal spectrum is too wide. The computed radial components and all derived values are invalid.
10	02000	The maximum of the averaged signal spectrum is smaller than the maximum of the averaged noise spectrum. The computed radial components and all derived values are invalid.
11	04000	The standard deviation as computed by the width of the averaged signal spectrum shows an imaginary value. If the atmospheric turbulence is very low (below 15 cm s^{-1}) this error message can occur frequently. The sigma-value must be set to zero.

